# On the Mass-Flux Representation of Vertical Transport in Moist Convection

PING ZHU

*Department of Earth and Environment, Florida International University, Miami, Florida*

(Manuscript received 10 November 2014, in final form 29 June 2015)

ABSTRACT

This study investigates to what extent the convective fluxes formulated within the mass-flux framework can represent the total vertical transport of heat and moisture in the cloud layer and whether the same approach can be extended to represent the vertical momentum transport using large-eddy simulations (LESs) of six well-documented cloud cases, including both deep and shallow convection. Two methods are used to decompose the LES-resolved vertical fluxes: decompositions based on the coherent convective features using the mass-flux top-hat profile and by two-dimensional fast Fourier transform (2D-FFT) in terms of wavenumbers. The analyses show that the convective fluxes computed using the mass-flux formula can account for most of the total fluxes of conservative thermodynamic variables in the cloud layer of both deep and shallow convection for an appropriately defined convective updraft fraction, a result consistent with the mass-flux dynamic view of moist convection and previous studies. However, the mass-flux approach fails to represent the vertical momentum transport in the cloud layer of both deep and shallow convection. The 2D-FFT and other analyses suggest that such a failure results from a number of reasons: 1) the complicated momentum distribution in the cloud layer cannot be well described by the simple top-hat profile; 2) shear-driven small-scale eddies are more efficient momentum carriers than coherent convective plumes; 3) the phase relationship between vertical velocity and horizontal momentum components is substantially different from that between vertical velocity and conservative thermodynamic variables; and 4) the structure of horizontal momentum can change substantially from case to case even in the same climate regime.

## 1. Introduction

How to appropriately represent the vertical transport of moist convection in large-scale models is a long-standing problem in weather forecasting and climate simulation and projection. The most common method to parameterize the convection-induced vertical transport is the mass-flux approach pioneered by Arakawa and Schubert (1974). In this framework, the total kinematic vertical flux of a generic variable $\chi$ at an arbitrary height may be decomposed into three parts,

$$\overline{w'\chi'} = \sigma\overline{w''\chi''}^{c} + (1-\sigma)\overline{w''\chi''}^{e} + \sigma(\overline{w}^{c} - \overline{w})(\overline{\chi}^{c} - \overline{\chi}) + (1-\sigma)(\overline{w}^{e} - \overline{w})(\overline{\chi}^{e} - \overline{\chi}), \quad (1)$$

where $\sigma$ is the fraction of coherent convective elements of an area. Overbars and overbars indexed with superscripts $c$ and $e$ indicate the averages over the area, the coherent convective elements, and the environment in which the coherent elements are embedded, respectively. Primes and double primes indicate the perturbations with respect to the domain mean and mean over the coherent convective elements and environment, respectively. To obtain Eq. (1), the top-hat distribution profile has been applied to the mean fields, that is, $\overline{\chi} = \sigma\overline{\chi}^{c} + (1-\sigma)\overline{\chi}^{e}$. The first and second terms on the right-hand side (RHS) of Eq. (1) represent the fluxes induced by the perturbations within the coherent convective elements and environment, respectively. The sum of the third and fourth terms on the RHS of Eq. (1) represents the fluxes induced by the coherent features associated with the convective elements and environment. One may further show that the third and fourth terms may be rewritten as

$$\langle w\chi\rangle_{c} = \sigma(\overline{w}^{c} - \overline{w})(\overline{\chi}^{c} - \overline{\chi}) + (1-\sigma)(\overline{w}^{e} - \overline{w})(\overline{\chi}^{e} - \overline{\chi}) = M_{c}(\overline{\chi}^{c} - \overline{\chi}^{e}), \quad (2)$$

where $\langle w\chi\rangle_{c}$ is known as the kinematic convective vertical flux of the variable $\chi$, and $M_{c} = \sigma(1-\sigma)(\overline{w}^{c} - \overline{w}^{e})$ is the kinematic convective mass flux.

*Corresponding author address*: Ping Zhu, Department of Earth and Environment, Florida International University, 11200 SW 8th Street, AHC-5 360, Miami, FL 33199.
E-mail: zhup@fiu.edu

DOI: 10.1175/JAS-D-14-0332.1

The concept of mass flux provides a concise description of moist convection and a practical way to parameterize the convection-induced vertical transport in large-scale models. Using large-eddy simulations (LESs), Siebesma and Cuijpers (1995) and Wang and Stevens (2000) showed that the convective fluxes computed by Eq. (2) can account for 80%–90% of the total fluxes of conservative thermodynamic variables, such as liquid water potential temperature $\theta_l$ and total water mixing ratio $q_t$, in the cloud layer of shallow cumuli, indicating that Eq. (2) provides a good estimate of the vertical transport of heat and moisture associated with shallow cumulus clouds. The mass-flux approach was originally developed for parameterizing deep cumulus convection and has been widely accepted by the community. Recently, Liu et al. (2015) examined the mass-flux representation of vertical transport of water vapor using the explicitly resolved fluxes by the cloud-resolving model (CRM) simulations of a midlatitude continental squall-line case and a tropical mesoscale convective complex case. However, although CRMs may appropriately simulate coherent convective features of deep moist convection, they cannot resolve large turbulent eddy circulations that are also important to the vertical transport. To the author's knowledge, no evaluation has been done at the LES scale to examine to what extent the convective fluxes computed by Eq. (2) can represent the total vertical transport of heat, moisture, and hydrometeors in the cloud layer of deep convection. In recent studies of mass-flux parameterization of deep moist convection, Arakawa and Wu (2013) and Wu and Arakawa (2014) developed a generalized mass-flux framework for cumulus parameterization. Their proposed "unified parameterization" framework eliminates the assumption of $\sigma \ll 1$ used by the traditional mass-flux parameterization to allow for a smooth transition to an explicit simulation of cloud-scale processes as the resolution increases. But the accuracy of using convective fluxes computed by Eq. (2) to represent the total vertical transport of heat and moisture in the cumulus layer is not discussed in their papers.

The vertical transport of horizontal momentum induced by moist convection is another important subgrid-scale process that needs to be represented in large-scale models. The importance of vertical transport of horizontal momentum induced by moist convection to large-scale circulations has been long recognized since the 1970s (e.g., Houze 1973; Riehl and Soltwisch 1974; Stone et al. 1974; Schneider 1975). Most of our knowledge on convective transport of horizontal momentum is also obtained in the mass-flux framework. Assuming that horizontal momentum components behave in the same manner as that of conservative thermodynamic variables, the kinematic convective momentum fluxes may be written as

$$\langle wu \rangle_c = M_c(\overline{u}^c - \overline{u}^e) \quad \text{and} \quad \langle wv \rangle_c = M_c(\overline{v}^c - \overline{v}^e), \tag{3}$$

where $u$ and $v$ are the horizontal wind components in a local Cartesian coordinate. Equation (3) has been extensively used in previous studies on the vertical momentum transport induced by deep moist convection, such as momentum budget analyses (e.g., Tung and Yanai 2002a,b) and cumulus parameterizations that include the effect of convective momentum transport (e.g., Schneider and Lindzen 1976; Zhang and Cho 1991a,b; Wu and Yanai 1994; Kershaw and Gregory 1997; Zhang and Wu 2003; Song et al. 2008; Wu et al. 2007). However, the vertical transport of horizontal momentum can be significantly different from the vertical transport of conservative thermodynamic variables because horizontal momentum is a vector with two independent nonconservative components. Whether Eq. (3) can appropriately account for the vertical momentum transport in the cloud layer of moist convection has not been discussed or evaluated by previous studies on mass-flux parameterization. Such an evaluation is important for two reasons. First, a convective or stratiform cloud regime usually has a well-defined vertical thermodynamic structure, whereas the mean vertical profiles of horizontal momentum may vary substantially from case to case even in the same climate regime. Thus, it is unclear if the mass-flux formula originally derived based on the thermodynamic fields can be appropriately extended to the dynamic fields. Second, researchers in other areas have shown that the momentum transport behaves differently from the transport of heat and moisture. For example, studies show that the coherent large turbulent eddies, such as roll vortices and convective cells, which can effectively transport heat and moisture in the atmospheric boundary layer (ABL), are inefficient in transporting momentum in the surface layer, that is, the lowest layer of the ABL (e.g., Townsend 1961; Bradshaw 1967; Shaw and Businger 1985; Mahrt and Gibson 1992; Högström and Bergström 1996; Zhu et al. 2010). For this reason, these large turbulent eddies are often called "inactive" eddies in literature. It was found that the intermittent smaller-scale eddies, such as "bursts/sweeps" or "gust microfronts" with scales of 10–100 m, are the efficient momentum carriers in the surface layer. Although turbulent mixing and its induced transport in the surface layer have different characteristics from the convection-induced vertical fluxes in the cloud layer, the findings of turbulent transport in the surface layer suggest that the vertical momentum transport could substantially differ from the

heat and moisture transport in the cloud layer. But no studies so far have investigated this issue.

Therefore, the motivations of this study are to advance our understanding of vertical transport processes in the cloud layer of moist convection and to distinguish the differences between vertical transport of horizontal momentum and vertical transport of conservative thermodynamic variables. To do so, LESs of a number of well-documented and studied cloud cases are performed. The generated numerical data allow us to quantify the individual contributions of explicitly simulated atmospheric flow from turbulent eddies to coherent convective features to the vertical transport of heat, moisture, and momentum in the cloud layer, and to evaluate to what extent the convective fluxes of conservative thermodynamic variables and horizontal momentum components computed by Eq. (2) can represent the total fluxes in the cloud layer of both deep and shallow moist convection. Specifically, this paper attempts to answer the following questions: 1) How much of total fluxes of conservative thermodynamic variables in the cloud layer of both deep and shallow convection can be represented by the convective fluxes computed by the mass-flux formula? 2) Can the mass-flux approach be extended to represent the vertical momentum transport in the cloud layer? 3) How does the partition of total fluxes of dynamic and thermodynamic variables based on the mass-flux top-hat profile differ from the flux decomposition in terms of eddy scales? The paper is organized as follows. Section 2 describes the LES setup and cloud cases simulated in this study. The simulation and analysis results are presented in section 3 followed by a summary of this study.

## 2. LES setup and cloud cases

Six well-documented and studied cloud cases are investigated in this study. These include four shallow cloud cases and two deep convective cases. The shallow cloud cases are the Barbados Oceanographic and Meteorological Experiment (BOMEX) case (Siebesma and Cuijpers 1995), the Rain in Cumulus Over the Ocean (RICO) case (VanZanten et al. 2011), the Atlantic Stratocumulus Transition Experiment (ASTEX) case (Bretherton et al. 1999), and the Second Dynamics and Chemistry of the Marine Stratocumulus field study (DYCOMS II), first research flight (RF01) case (Stevens et al. 2005; Zhu et al. 2005). These cases provide a good representation of maritime boundary layer (MBL) clouds over the vast ocean under different climatological conditions from typical trade wind shallow cumulus and shallow clouds in transition regions to stratocumulus capped by a strong sharp inversion. Note that the parameterization of stratocumulus in large-scale models is not based on the mass-flux approach. The reason to include the stratocumulus case DYCOMS-II-RF01 in this study is to compare the vertical transport process in stratiform clouds with that in the convective clouds. The initial profiles, surface conditions, and large-scale forcing of these four cases can be found in the corresponding references provided in the paper. The simulations of all four cases are forced by the prescribed surface fluxes. The BOMEX and RICO cases are run for 6 h, and the ASTEX and DYCOMS-II-RF01 cases are run for 9 h. Since all four simulations reach the quasi-steady steady after the initial spinup period due to the prescribed surface forcing used in the simulations, the model outputs from the last 3 h are used for analysis.

As stated previously, small-scale turbulence may play an important role in momentum transport; thus, to understand the momentum transport processes in the cloud layer, high-resolution LESs are needed to resolve a range of scales from small-scale turbulence to coherent convective features. Combining this consideration and our computational ability, the model horizontal grid spacing used for all four cases is set to 25 m with a horizontal grid mesh of $640 \times 640$ covering an area of $16 \times 16\,\mathrm{km}^2$. The vertical grid spacing is set to 20 m for the three shallow cumulus cases and 5 m in the cloud layer for the stratocumulus case, DYCOMS-II-RF01. The model top varies from case to case, but it is set to the height well above the cloud layer.

The two deep convective cases are selected from the Tropical Ocean and Global Atmosphere Coupled Ocean–Atmosphere Response Experiment (TOGA COARE; Webster and Lukas 1992) and the GARP Atlantic Tropical Experiment (GATE; Mason 1975). The domain size of $16 \times 16\,\mathrm{km}^2$ used for simulating shallow cloud cases is too small to realistically simulate deep convective cloud cases, but the available computational resources do not allow for a substantial increase in the model grid mesh. As a compromise, the horizontal grid spacing is increased to 100 m but the grid mesh of $640 \times 640$ is still kept the same so that the model domain covers an area of $64 \times 64\,\mathrm{km}^2$. The vertical grid spacing is also increased, 50 m below 2 km and then gradually increasing to 150 m until the model top at 23.3 km. Such an increase of model grid spacing may be acceptable for deep convection because convective elements are much stronger than those of shallow convection, and thus presumably the relative importance of turbulent eddies may be reduced. From the turbulent energy spectrum perspective, large turbulent eddies are energy-containing eddies. A key requirement of an LES is that the model grid spacing should fall in the inertial subrange, so that the model explicitly simulates large

energy-containing eddies while parameterizing small eddies that are more isotropic and less flow dependent. It is, thus, unclear if the simulated results will be substantially affected because of the reduced model resolution. However, according to Bryan et al. (2003), 100-m horizontal resolution seems to be sufficient for a realistic simulation of deep moist convection. In a recent LES study of GATE convection by Khairoutdinov et al. (2009), a 100-m grid spacing is also used but with a much larger grid mesh of $2048 \times 2048 \times 256$. The statistics of some key variables from the GATE simulation performed in this study appears to be consistent with those from Khairoutdinov et al.'s (2009) "Giga-LES" (see Fig. 2), suggesting that the smaller horizontal grid mesh ($640 \times 640$) used in this study is acceptable. The simulation of the TOGA COARE case starts at 1800 UTC 18 December 1992, and the GATE case is selected from phase III starting at 0000 UTC 1 September 1974. Both simulations are executed for 24 h in which the surface fluxes are determined interactively based on the prescribed sea surface temperature (SST). Figure 1 shows the initial vertical profiles, large-scale forcing, and SST used for the simulations of the two deep cases. Note that different forcing strategies are used for the GATE and TOGA COARE simulations. In the GATE simulation, the total tendencies of temperature and moisture are imposed, whereas the horizontal advective tendencies and large-scale vertical velocity are imposed in the TOGA COARE simulation. However, to make an appropriate comparison of large-scale forcings between the two simulations, the total tendencies for the TOGA COARE case are plotted in Fig. 1. The large-scale forcing for the GATE and TOGA COARE simulations were derived from field experiments and are the same as those used in previous numerical simulations (e.g., Xu and Randall 1996; Grabowski et al. 1996; Wu et al. 1998; Redelsperger et al. 2000; Mechem and Oberthaler 2013). As shown in Figs. 1e–h, the large-scale forcing of the TOGA COARE case is stronger than that of the GATE case. The selection of deep convective cases with relatively weak and strong large-scale forcing is based on the consideration that the goal of this study is to evaluate the extent that the basic assumption of mass-flux approach is valid for convection under different forcing conditions over the vast tropical and subtropical ocean. Nonetheless, the peak total tendencies of the GATE case (Figs. 1e and 1g) are comparable to the mean GATE large-scale forcing used by Khairoutdinov et al. (2009). Table 1 summarizes the basic model configurations of the six cloud cases simulated in this study. Nudging is not activated in all six cases. This is based on the consideration that the focus of this study is on investigating vertical transport processes associated with moist convection, and thus a fully free development of eddy circulations with different scales is most important. All LESs are performed by the System for Atmospheric Modeling (SAM). For detailed information of model dynamics and physics, please refer to Khairoutdinov and Randall (2003). Three-dimensional data are collected at a 2-min interval. In this study, the domain size for shallow and deep moist convection is $16 \times 16\,\mathrm{km}^2$ and $64 \times 64\,\mathrm{km}^2$, respectively. For all cases investigated in this study, the mean wind speed below 10 km is less than $10\,\mathrm{m\,s}^{-1}$. Thus, the eddy residence time for shallow and deep convection is 26.7 and 106.7 min, respectively, assuming the advection speed is $10\,\mathrm{m\,s}^{-1}$. This indicates that 2-min output can sample an eddy in the domain sufficient times to obtain reliable statistics. The comparison of several key variables (e.g., wind components, thermodynamic variables, and hydrometeors) shows that the statistics calculated from the 2-min output is nearly identical to the SAM online statistics that collects samples at each time step. Since the two-dimensional fast Fourier transform (2D-FFT) performed in this study (to be shown later) uses the 2-min model output, for consistency all analyses presented in this paper are done using the 2-min model output.

## 3. Analysis results

Unlike the four shallow cloud cases, which are forced by the constant surface fluxes, the surface fluxes in the simulations of the two deep convection cases are determined interactively based on the prescribed SST; thus, a quasi-steady state cannot be reached. Rather, the simulated convection shows a substantial temporal variation. Figures 2a–d show the time evolution of simulated cloudy updraft mass flux, surface rainfall, and surface buoyancy fluxes $\rho C_p \overline{w'\theta'_{v0}}$ of the GATE and TOGA COARE cases, where $\rho$, $C_p$, and $\theta_v$ are air density, specific heat at constant pressure, and virtual potential temperature, respectively. The subscript 0 indicates the value at the surface. There is a strong deep convective episode in the 24-h simulation of each case. In both cases, the initiation of the deep convection episode matches well with the increase of surface buoyancy fluxes. The maximum surface rainfall of the GATE case reaches $24\,\mathrm{mm\,day}^{-1}$, which does not appear to be small considering the relatively weak large-scale forcing imposed and is comparable to the surface rainfall of Khairoutdinov et al.'s (2009) simulation in which the mean GATE forcing is imposed. Since these two cases are selected mainly for understanding the vertical transport processes of deep convection, our analyses below will focus on the two strong deep convective

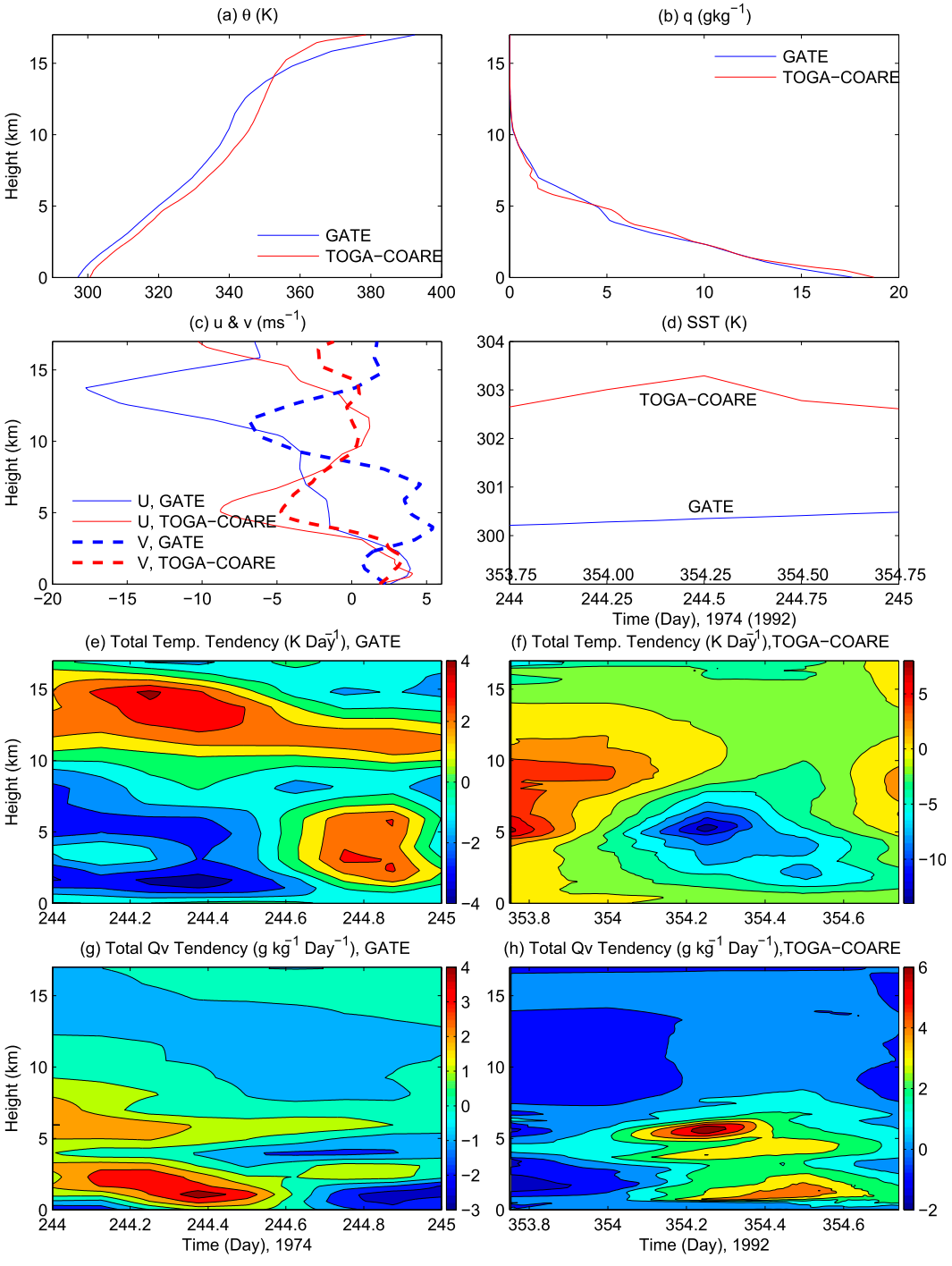


FIG. 1. Initial vertical profiles and large-scale/surface forcing of GATE and TOGA COARE. (a) Initial potential temperature $\theta$. (b) Initial water vapor mixing ratio $q$. (c) Initial $x$-direction and $y$-direction wind components. (d) Sea surface temperature. Total temperature tendencies for (e) GATE and (f) TOGA COARE. Total moisture tendencies for (g) GATE and (h) TOGA COARE.

episodes marked by the white vertical lines in Figs. 2a and 2b. Each episode lasts approximately 3 h.

To further assess the fidelity of the simulations of the two deep convective cases, Figs. 2e–h show the vertical profiles of several key variables describing the main characteristics of moist convection averaged over the convective episodes of GATE and TOGA COARE defined in Figs. 2a and 2b, where an updraft core is

TABLE 1. Basic model configuration of six cloud cases.

| | Horizontal grid spacing (m) | Vertical grid spacing | Grid mesh | Surface forcing | Simulation duration (h) |
|---|---|---|---|---|---|
| BOMEX | 25 | 20 m | 640 × 640 × 180 | Prescribed fluxes | 6 |
| RICO | 25 | 20 m | 640 × 640 × 180 | Prescribed fluxes | 6 |
| ASTEX | 25 | 20 m | 640 × 640 × 156 | Prescribed fluxes | 9 |
| DYCOMS-II-RF01 | 25 | 10 m (below 500 m)<br>5 m (500–1050 m)<br>10 m (above 1050 m) | 640 × 640 × 180 | Prescribed fluxes | 9 |
| GATE | 100 | 50 m (below 2 km)<br>50–150 m (above 2 km) | 640 × 640 × 186 | Prescribed SST | 24 |
| TOGA COARE | 100 | 50 m (below 2 km)<br>50–150 m (above 2 km) | 640 × 640 × 186 | Prescribed SST | 24 |

defined to have vertical velocity greater than $1\,\mathrm{m\,s^{-1}}$ for 500 m or more. This definition of core is the same as that used by Khairoutdinov et al. (2009). The updraft core vertical velocity, updraft core mass flux, cloud fraction, and precipitation flux of the GATE case have similar magnitude and vertical structure to those of Khairoutdinov et al. (2009). There are two major differences between the two simulations. One is that the convection in Khairoutdinov et al.'s (2009) simulation is a little deeper than the GATE simulation performed in this study. The other is that cloud fraction above 5 km in our simulation shows a double-layered structure, which is not shown in Khairoutdinov et al.'s (2009) simulation. These differences may be attributed to the different large-scale and surface forcing used in the simulations and should not affect the vertical transport analyses and main conclusions presented in this paper. While the vertical profiles of these variables from the TOGA COARE simulation share the main characteristics of the GATE simulation, they do show some interesting differences. One of them is the cloud fraction, which remains small at most of the altitudes in the TOGA COARE simulation except for the cloud top near 15 km. The impact of this difference in cloud fraction on vertical transport will be discussed in detail shortly. The statistics of these key variables from our TOGA COARE simulation is qualitatively consistent with that of Mechem and Oberthaler (2013), who simulated 20 days of TOGA COARE but used 200-m horizontal resolution and a grid mesh of 512 × 128 × 165, which is much smaller than the grid mesh of 640 × 640 × 186 used in this study. The good convection simulations summarized in Figs. 2e and 2h suggest that the numerical data generated in this study are appropriate for investigating the vertical transport processes of deep moist convection.

Using Eq. (1), the LES-resolved kinematic vertical fluxes of $\theta_l$, $q_t$, and horizontal momentum components (i.e., $\overline{w'\theta_l'}$, $\overline{w'q_t'}$, $\overline{w'u'}$, and $\overline{w'v'}$) are decomposed into the three parts associated with the coherent convective features and the perturbations within the coherent features and environment. Three different ways are used to define the coherent features in the cloud layer. These include the coherent features defined based on 1) clouds ($q_c > 0.001\,\mathrm{g\,kg^{-1}}$), 2) cloud updraft ($q_c > 0.001\,\mathrm{g\,kg^{-1}}$ and $w > 0.01\,\mathrm{m\,s^{-1}}$), and 3) cloud buoyant core ($q_c > 0.001\,\mathrm{g\,kg^{-1}}$ and $\theta_v' > 0$), where $q_c$, $w$, and $\theta_v$ are the cloud water mixing ratio, vertical velocity, and virtual potential temperature, respectively. Figures 3 and 4 show the mean vertical profiles of $\overline{w'\theta_l'}$ and $\overline{w'q_t'}$ determined directly from the model output using the eddy correlation method along with the three components decomposed based on the coherent features defined by the cloud updraft averaged over the last three simulation hours for the shallow cloud cases and over the strong deep convection episode of the two deep convection cases. For all the cloud cases except for the GATE case, the convective fluxes computed by Eq. (2) have a vertical structure and magnitude very close to those of the LES-resolved fluxes in the cloud layer. This result supports the classic view of moist convection that coherent updrafts–downdrafts are mainly responsible for the vertical transport in the cloud layer and is consistent with what has been found in the previous LES studies of shallow convection. It confirms that the vertical transport of conservative thermodynamic variables in the cloud layer can be well represented by Eq. (2). The decomposition of fluxes based on clouds and the cloud buoyant core defined previously shows similar characteristics (not shown here), but the convective fluxes do not match the LES-resolved fluxes in the cloud layer as closely as those determined by the cloud updraft. The substantial underestimation of the LES-resolved fluxes of $\theta_l$ and $q_t$ by the convective fluxes computed by Eq. (2) of the GATE case is a surprise considering that the application of the mass-flux approach to deep convection is widely accepted by the community. The underlying reason for the poor representation of the vertical transport of

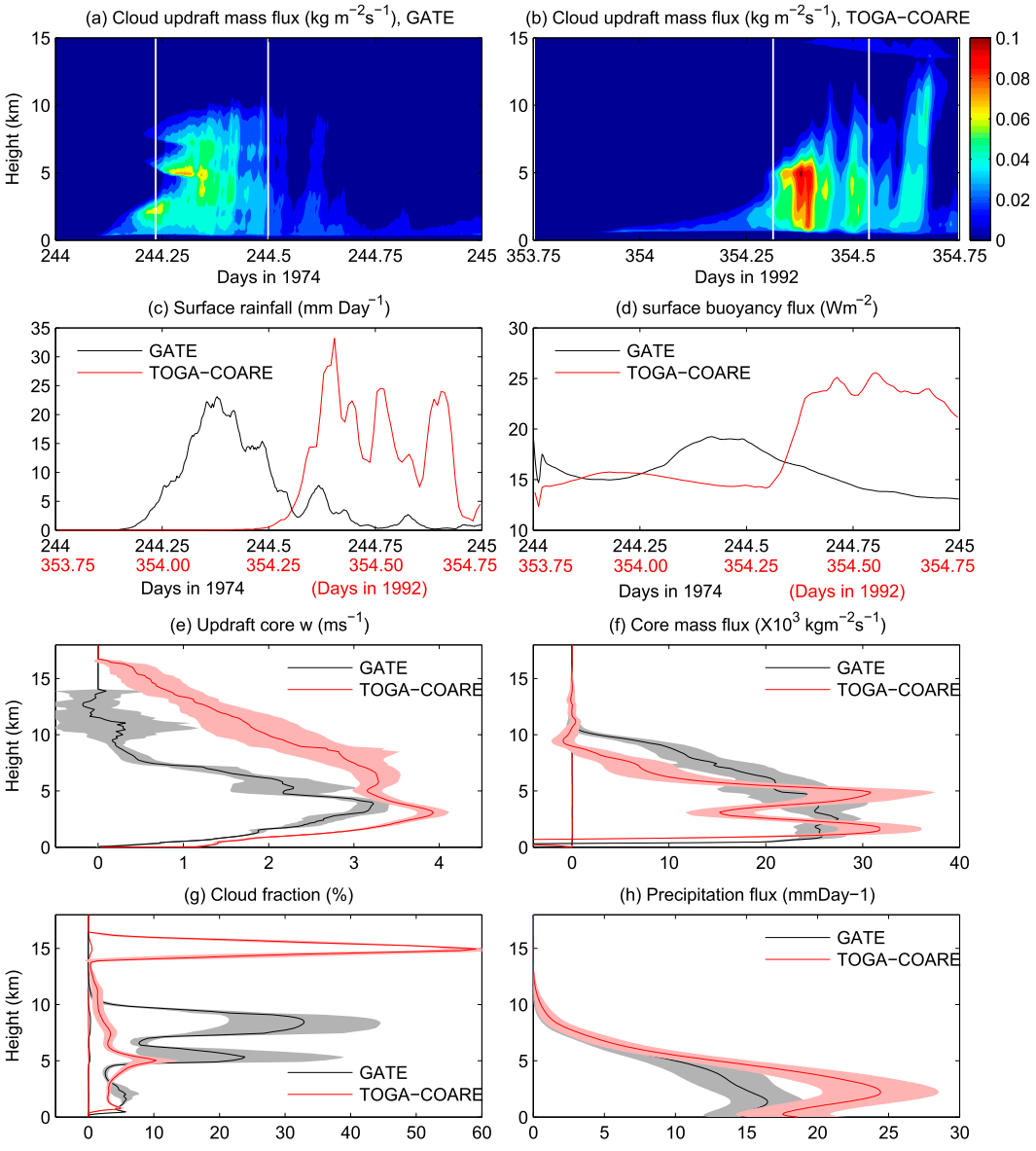


FIG. 2. Time evolution of domain-mean simulated cloud updraft mass flux of (a) GATE and (b) TOGA COARE, (c) domain-mean surface rainfall, and (d) domain-mean surface buoyancy fluxes of GATE and TOGA COARE. White vertical lines in (a) and (b) denote the time periods analyzed in this study. Black and red curves in (c) and (d) are scaled by the black and red $x$ axes, respectively. (e)–(h) Domain-mean vertical profiles of vertical velocity (m s$^{-1}$) in the updraft core, mass flux ($\times 10^3$ kg m$^{-2}$ s$^{-1}$) of the updraft core, cloud fraction (%), and precipitation flux (mm day$^{-1}$), respectively, averaged over the deep convective episode indicated by the vertical white lines in (a) and (b) for GATE and TOGA COARE. An updraft core is defined to have vertical velocity $>1$ m s$^{-1}$ for 500 m and more. The shades indicate the standard deviations of the domain-mean vertical profiles over the episode of interest.

conservative thermodynamic variables in the cloud layer by the mass-flux approach in this case will be explored shortly.

The decomposition of momentum fluxes (Figs. 5 and 6) shows a different story from that of $\overline{w'\theta_l'}$ and $\overline{w'q_t'}$. The convective momentum fluxes estimated by Eq. (3) provide a poor estimate of the LES-resolved vertical momentum transport in the cloud layer for all shallow and deep cloud cases. For shallow cumulus cases (BOMEX and RICO), although the $x$-direction component of convective momentum fluxes computed by Eq. (3) appears to have a similar vertical structure to that of the LES-resolved momentum fluxes in the cloud layer (Figs. 5a and 5b), the $y$-direction component of momentum fluxes induced by coherent features is far off from the $y$-direction momentum fluxes resolved by the

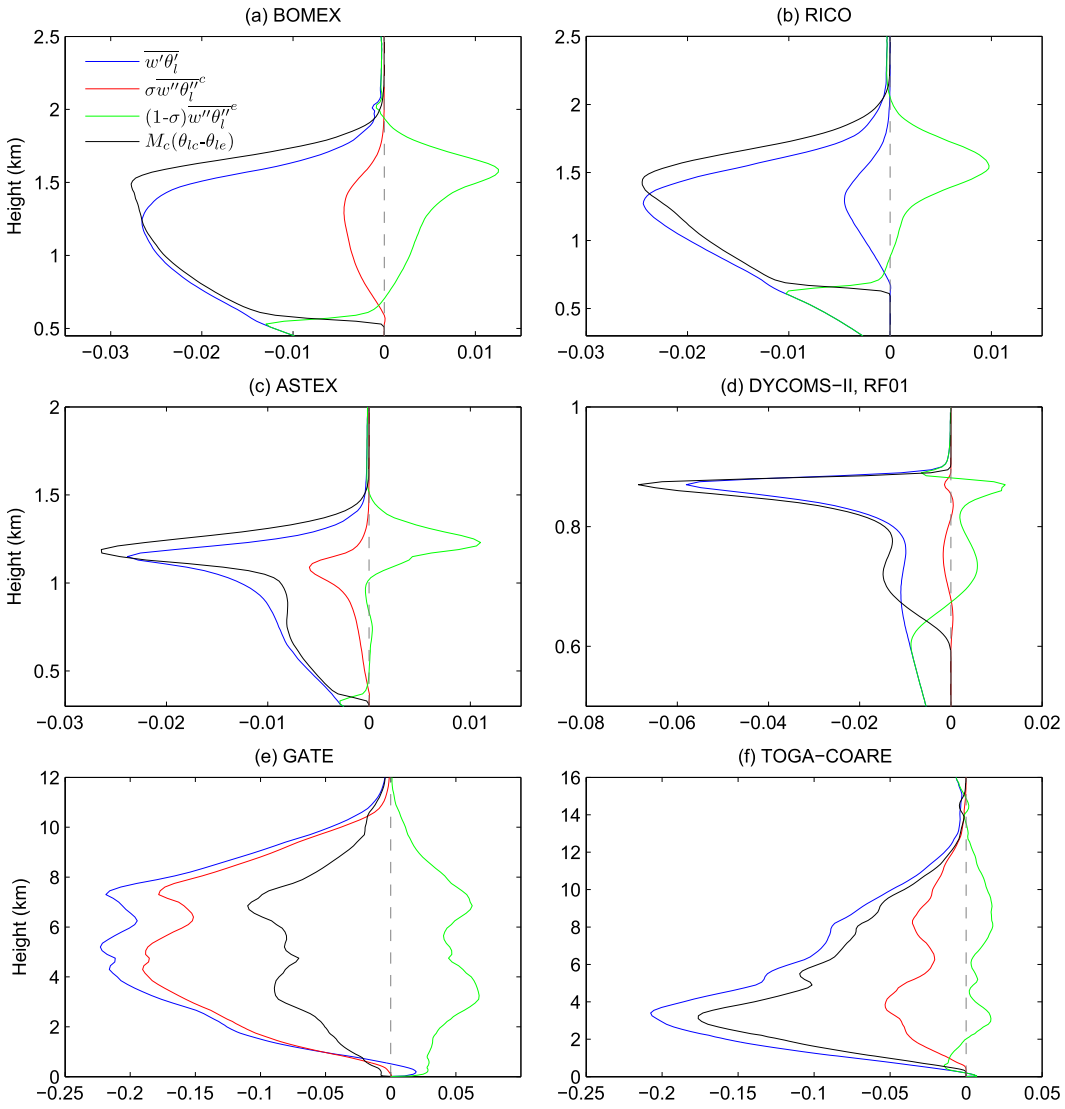


FIG. 3. Decomposition of the vertical fluxes of liquid water potential temperature (K m s$^{-1}$) using Eq. (1) based on the coherent cloud updraft defined by $q_c > 10^{-3}$ g kg$^{-1}$ and $w > 0.01$ m s$^{-1}$ of the six cloud cases. Blue, black, red, and green curves denote the total fluxes resolved by LES, convective fluxes associated with the coherent features computed by Eq. (2), flux components induced by the perturbations inside the coherent features, and environment in which the coherent features are embedded, respectively. The dashed line indicates the zero line. The profiles are averaged over the last 3 h for shallow cloud cases and the convective episode of deep cloud cases, GATE and TOGA COARE, indicated respectively, in Figs. 2a and 2b.

LES (Figs. 6a and 6b). The situation for the stratocumulus (DYCOMS-II-RF01) case is opposite. The coherent convective features appear to account for most of the resolved *y*-direction momentum fluxes (Fig. 6d), but the *x*-direction component of convective momentum fluxes computed from Eq. (3) deviates substantially from the LES-resolved *x*-direction momentum fluxes in the cloud layer (Fig. 5d). For shallow cumulus in the transition (ASTEX), the convective fluxes computed from Eq. (3) provide a poor estimate of the LES-resolved momentum fluxes in both directions in the cloud layer (Figs. 5c and 6c). In the deep convective TOGA COARE case, although the convective momentum fluxes computed by Eq. (3) appears to provide a good estimate of the *x*-direction momentum fluxes resolved by the LES, particularly in the mid- to upper-cloud layer (Fig. 5f), they do not represent well the *y*-direction momentum fluxes (Fig. 8f). In the deep convective GATE case, the convective momentum fluxes computed by Eq. (3) completely fail to represent the LES-resolved vertical momentum fluxes in both the *x* and *y* directions (Figs. 5e and 6e). The result shown in

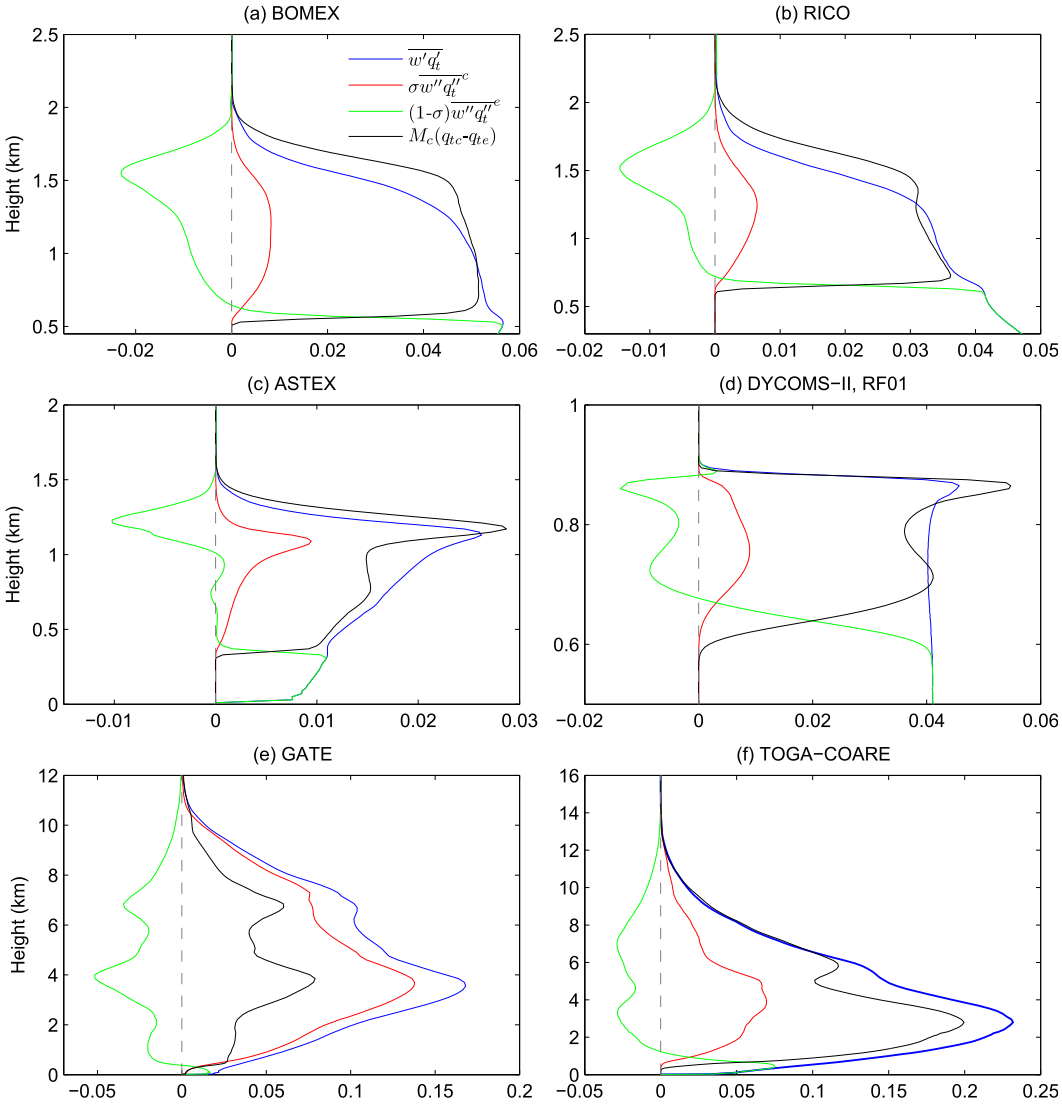


FIG. 4. As in Fig. 3, but for the vertical fluxes of the total water mixing ratio ($g\,kg^{-1}\,m\,s^{-1}$).

Figs. 5 and 6 indicates that in general the convective fluxes computed using the mass-flux formula do not provide a good estimate of the LES-resolved vertical momentum fluxes in the cloud layer of both deep and shallow convection, although good matches of the two fluxes may be found occasionally in some cases.

The different performance of the mass-flux formula in representing the total vertical fluxes of conservative thermodynamic variables and horizontal momentum components should reflect the fundamental difference in governing vertical transport of conservative scalar and nonconservative momentum induced by eddy circulations. Physically, all convective clouds are developed from thermal plumes or cells originated at the surface that have similar thermodynamic properties. During adiabatic rising, the convective plumes or cells conserve their reversible thermodynamic properties, such as liquid water potential temperature and total water mixing ratio, to a good approximation, implying that there should be a good correlation between updraft and conserved thermodynamic properties. This suggests that most of the vertical transport of conservative thermodynamic variables should be carried out by a few strong convective updrafts. However, convective plumes or cells do not necessarily possess similar properties of horizontal momentum components since thermal plumes or cells are generated mainly due to inhomogeneous heating but not by dynamic forcing. Therefore, inside a plume updraft, momentum components may have a large variation leading to both positive and negative momentum perturbations (i.e., $+u'$, $-u'$, $+v'$, and $-v'$), so that the cancellation of

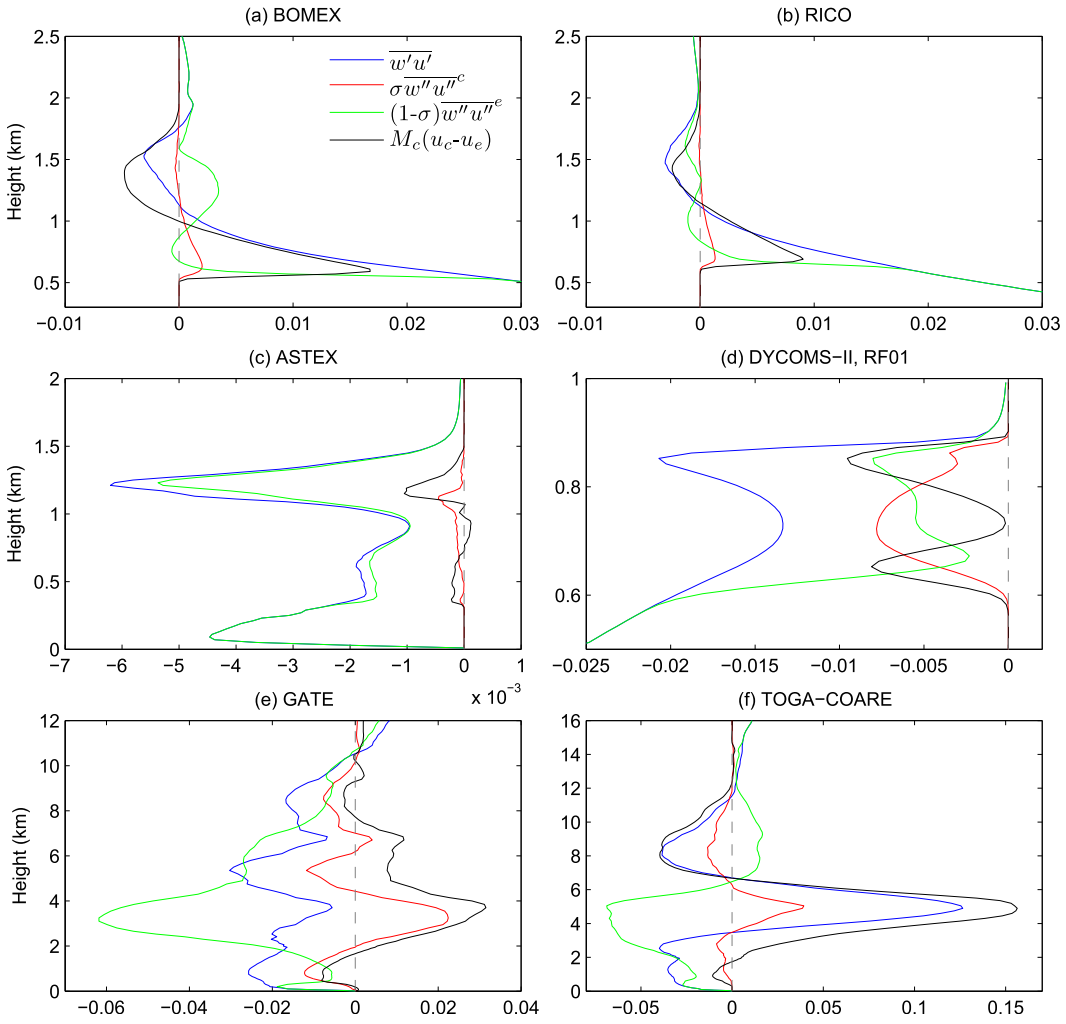


FIG. 5. As in Fig. 3, but for the vertical fluxes of the $x$-direction wind component ($m^2\,s^{-2}$).

positive and negative $w'u'$ and $w'v'$ within the plume updraft may result in small net momentum fluxes. Moreover, as pointed out by Wu and Arakawa (2014), horizontal momentum components are not conservative variables due to the pressure gradient force. Hence, as convective updrafts rise, the change in momentum components can lead to further changes in momentum fluxes from height to height. From the mechanism of an eddy-generation perspective, in addition to buoyancy production, eddy circulations can also be generated by dynamic instabilities, such as the Kelvin–Helmholtz instability due to wind shear, which tends to produce small-scale eddies. The updrafts/downdrafts of small eddies are effective in vertical momentum transport, as they can generate large momentum fluxes, $w'u'$ and $w'v'$. The small shear-driven eddies overlapped onto the relative large convectively driven plumes or cells provide an explanation of the difference between the vertical transport of conservative thermodynamic variables and the vertical transport of nonconservative horizontal momentum seen in the simulations.

The difference in mass-flux decomposition of vertical fluxes of conservative thermodynamic variables in the two deep convection cases shown in Figs. 3e, 3f, 4e, and 4f is interesting. Analyses show that the substantial underestimation of the LES-resolved fluxes of $\theta_l$ and $q_t$ by the convective fluxes computed by Eq. (2) in the GATE case is mainly due to the large fraction of cloud updraft defined by $q_c > 0.001\,g\,kg^{-1}$ and $w > 0.01\,m\,s^{-1}$ used for flux decomposition. As an illustration, Figs. 7a–f show the time series of simulated vertical fluxes of total water mixing ratio $q_t$, cloud updraft fraction defined by different thresholds of vertical velocity ($q_c > 0.001\,g\,kg^{-1}$ and $w > 0.01\,m\,s^{-1}$ and $q_c > 0.001\,g\,kg^{-1}$ and $w > 0.7\,m\,s^{-1}$), and the ratios of convective fluxes to the total resolved fluxes of $q_t$ corresponding to the different cloud updraft thresholds at 5-km altitude of the GATE case compared with those obtained from the

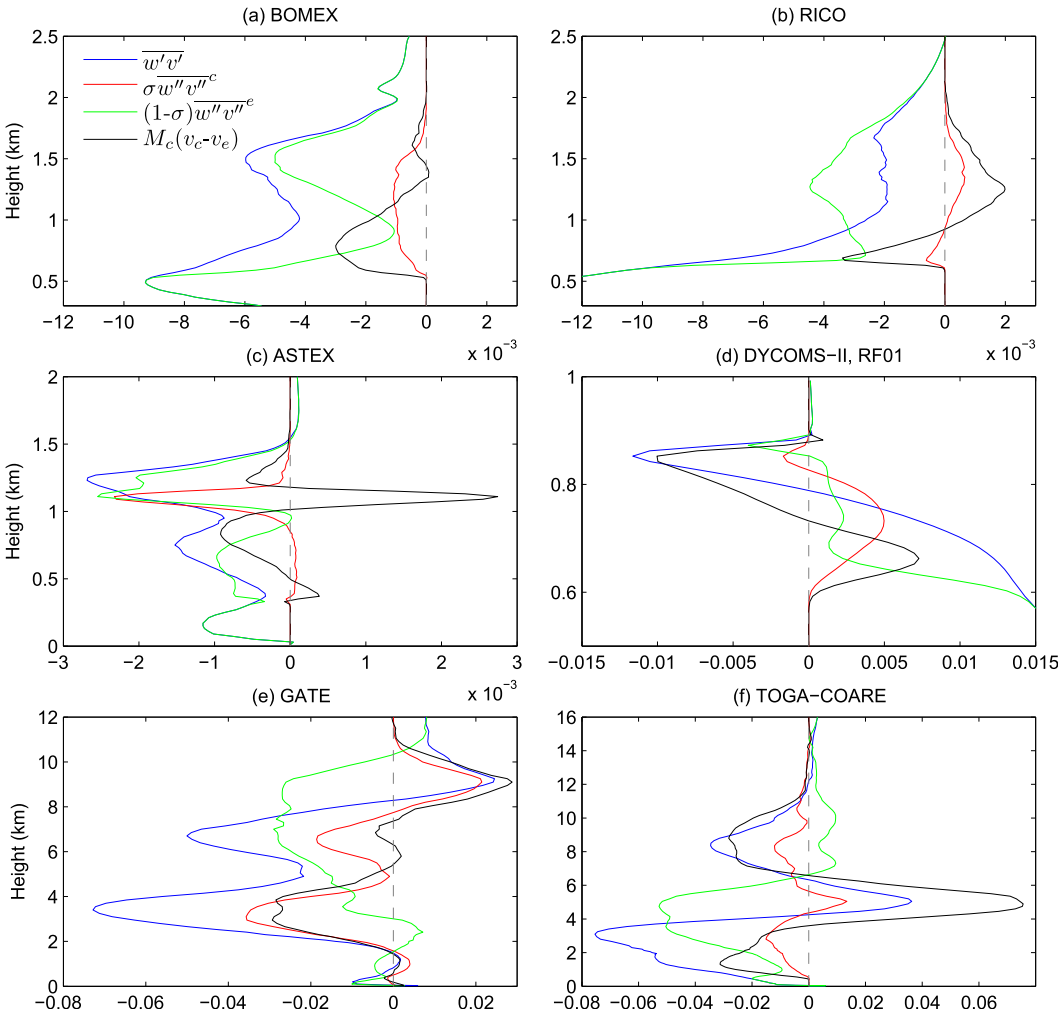


FIG. 6. As in Fig. 3, but for the vertical fluxes of the $y$-direction wind component ($m^2\,s^{-2}$).

TOGA COARE case. The time evolution of the convective updraft fraction defined by $q_c > 0.001\,g\,kg^{-1}$ and $w > 0.01\,m\,s^{-1}$ in the two cases shows a similar characteristic; that is, a peak fraction occurs at an early time during the simulations, which is most likely associated with the model spinup. After the peak, the convective updraft fraction decreases and then reaches a quasi-steady state. In the TOGA COARE case, the convective updraft fraction after the spinup is consistently smaller than 5%, whereas the convective updraft fraction after the spinup in the GATE case is around 10%. The convective fluxes associated with the cloud updraft computed by Eq. (2) are able to account for most of the LES-resolved fluxes after the spinup period (about 70%–100%) in the TOGA COARE case, but they substantially underestimate the LES-resolved fluxes in the GATE case (less than 50%). We have done sensitivity experiments on the flux decomposition using different thresholds of vertical velocity to define the coherent convective features. The results show that the ratio of the convective fluxes computed by Eq. (2) to the LES-resolved fluxes consistently increases as the vertical velocity threshold increases. When the vertical velocity threshold increases to $0.7\,m\,s^{-1}$, the convective updraft fraction in the GATE case reduces to the value similar to that of the TOGA COARE case (Figs. 7c and 7d). As a response, the ratio of the convective fluxes to the total resolved fluxes in the GATE case also increases to the value similar to that of the TOGA COARE case.

To further confirm the importance of the fraction of coherent convective elements to the mass-flux decomposition, Figs. 7g–j show the decomposition of the LES-resolved vertical fluxes of GATE using Eq. (1) based on the coherent cloud updraft defined by $q_c > 10^{-3}\,g\,kg^{-1}$ and $w > 0.7\,m\,s^{-1}$. Compared with Figs. 3–6, the representation of the LES-resolved fluxes of $\theta_l$ and $q_t$ by the corresponding convective fluxes is significantly improved (Figs. 7g and 7h). This result supports the

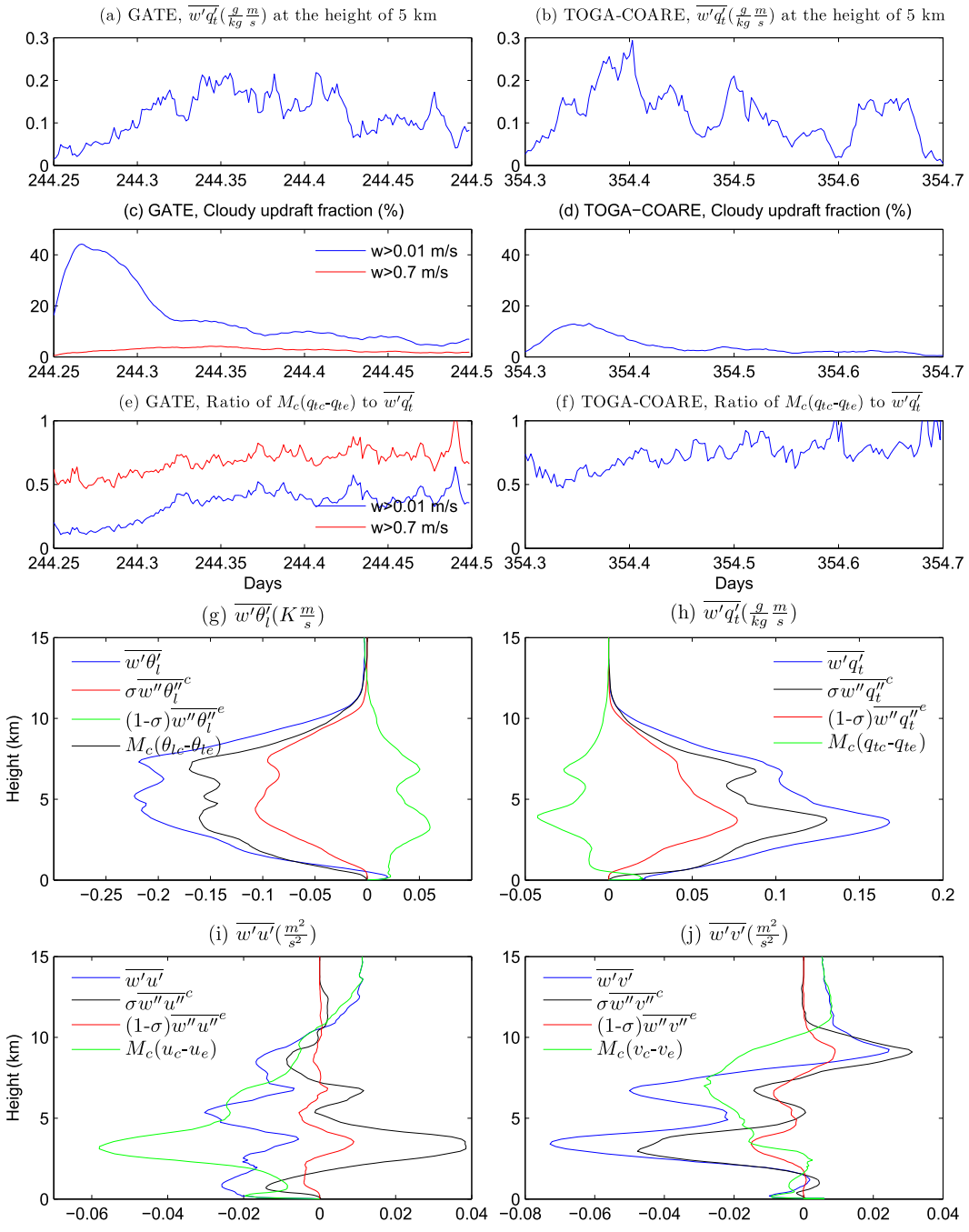


FIG. 7. Time series of domain-mean vertical fluxes of total water mixing ratio ($g\,kg^{-1}\,m\,s^{-1}$) at 5-km altitude for (a) GATE and (b) TOGA COARE. (c),(d) Cloud updraft fractions (%) at 5-km altitude for (c) GATE and (d) TOGA COARE. Blue and red curves indicate the cloud updraft fraction defined by $q_c > 10^{-3}\,g\,kg^{-1}$ and $w > 0.01\,m\,s^{-1}$ and $q_c > 10^{-3}\,g\,kg^{-1}$ and $w > 0.7\,m\,s^{-1}$, respectively. (e),(f) Ratio of convective fluxes to total resolved fluxes of total water mixing ratio at 5-km altitude for (e) GATE and (f) TOGA COARE. Blue and red curves indicate the ratio determined by the two differently defined cloud updrafts. (g)–(j) Decomposed vertical fluxes of GATE averaged over the convective episode indicated in Fig. 2. The decomposition is based on the cloud updraft defined by $q_c > 10^{-3}\,g\,kg^{-1}$ and $w > 0.7\,m\,s^{-1}$. The meaning of blue, black, red, and green curves is as in Figs. 3–6.

basic dynamic view of the mass-flux approach, that the organized structure consisting of strong updrafts and the associated downdrafts are mainly responsible for the vertical transport of conservative thermodynamic variables. When cloud updraft fraction is small, a few strong updrafts and the associated downdrafts can be well described by the mass-flux top-hat profile, and the contribution of the internal variation within the updrafts–downdrafts to the total transport [i.e., the first two terms in Eq. (1)] is negligible. However, as the convective updraft fraction becomes larger, the more complicated updraft–downdraft structure will be difficult to represent by the top-hat profile, and thus a higher chance for the mass-flux approach to fail. In this case, the large convective updraft fraction increases the internal variations within the updrafts and this is what we see in Figs. 3e and 4e—that the internal variation within the convective updraft contributes significantly to the total vertical fluxes of $\theta_l$ and $q_t$. It should be pointed out that the threshold of $0.01\,\mathrm{m\,s^{-1}}$ may be too small for defining the convective updrafts. Such defined updrafts under certain circumstances may include both convective and stratiform clouds that may have very different thermodynamic properties. For example, in a study of GATE deep convection, LeMone and Zipser (1980) used a threshold of $0.5\,\mathrm{m\,s^{-1}}$ to define the deep convective updraft. In the GATE case simulated in this study, a value of $0.7\,\mathrm{m\,s^{-1}}$ significantly improves the performance of the mass-flux approach. However, a much smaller threshold ($0.01\,\mathrm{m\,s^{-1}}$) of vertical velocity seems to work well for the TOGA COARE deep convective case and all shallow convective cases, suggesting that finding an appropriate vertical velocity threshold for defining the convective updraft in mass-flux parameterization is not scientifically trivial. Recently, Arakawa and Wu (2013) and Wu and Arakawa (2014) developed a unified mass-flux parameterization framework in which convective updraft fraction can be determined internally within the framework. Their study virtually provides a way to solve this problem. If the method for determining convective updraft fraction could appropriately account for the strong convective updrafts responsible for vertical transport, then the unified mass-flux system would significantly improve moist convection parameterization in large-scale models. Another possible method to solve this problem is to use multiple updrafts instead of a single updraft to encompass the complicated dynamic structure of moist convection. As shown by Arakawa and Wu (2013) and Liu et al. (2015), the mass-flux representation of vertical transport of heat and moisture can be improved by using multiple updrafts.

As a comparison, Fig. 8 shows the cloud updraft fraction defined by $q_c > 0.001\,\mathrm{g\,kg^{-1}}$ and $w > 0.01\,\mathrm{m\,s^{-1}}$

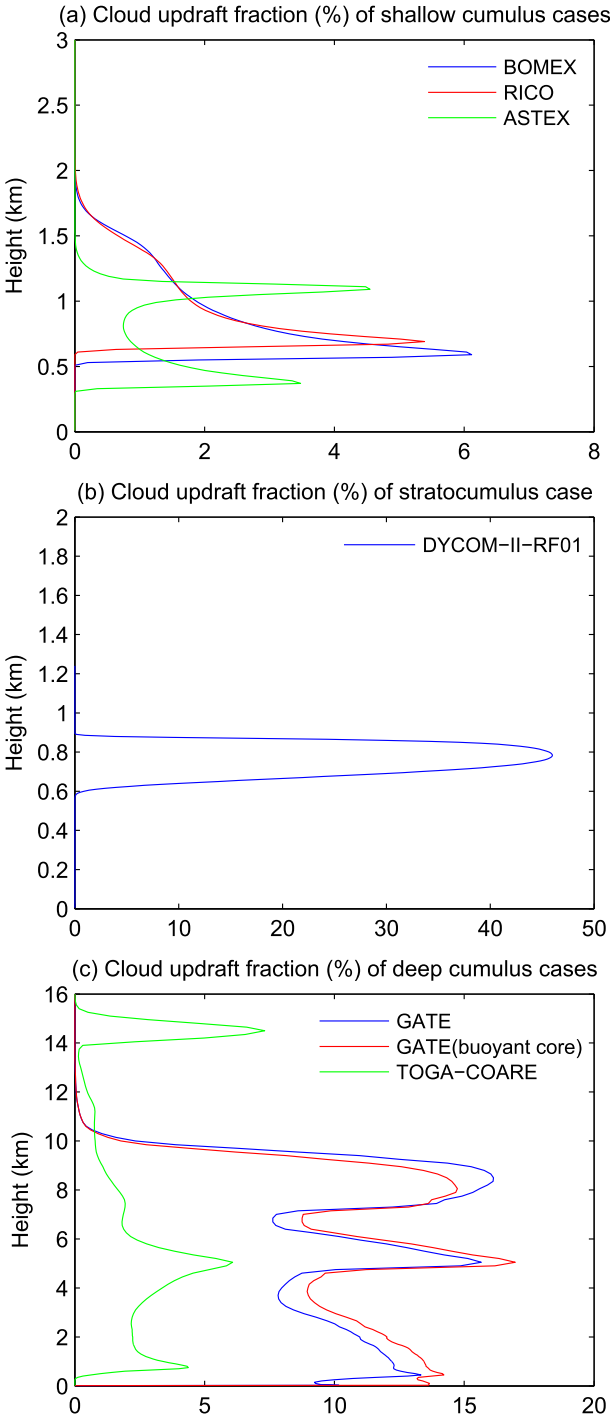


FIG. 8. Cloud updraft fractions defined by $q_c > 10^{-3}\,\mathrm{g\,kg^{-1}}$ and $w > 0.01\,\mathrm{m\,s^{-1}}$averaged over the last 3 h for shallow cloud cases and over the convective episode for deep cloud cases indicated in Fig. 2. The cloud buoyant core fraction defined by $\theta_v' > 0\,\mathrm{K}$ and $w > 0.01\,\mathrm{m\,s^{-1}}$ and $q_c > 10^{-3}\,\mathrm{g\,kg^{-1}}$ of GATE is also provided.

of the six cloud cases averaged over the same periods as those in Fig. 3. For all the cumulus convection cases (BOMEX, RICO, ASTEX, and TOGA COARE) except for the GATE case, the cloud updraft fraction is consistently smaller than 5%. In all these cases, the mass-flux convective fluxes represent well the total fluxes of $\theta_l$ and $q_t$ in the cloud layer. However, in the GATE case, both the cloud updraft fraction and cloud buoyant core (defined by $q_c > 0.001\,\mathrm{g\,kg^{-1}}$ and $\theta_v' > 0$) fraction are larger than 10%. The stratocumulus (DYCOMS-II-RF01) case shows a 45% cloud updraft fraction in a shallow cloud layer, suggesting that nearly half of the clouds are dominated by updraft, which is not unusual for stratocumulus clouds. Note that the mass-flux approach was not developed to parameterize the stratocumulus-induced vertical transport and that indeed in large-scale models the stratocumulus parameterization is often incorporated into the turbulent mixing scheme, such as the parameterizations used in the NCAR CAM5 and ECMWF models. But as we showed here, the mass-flux decomposition [Eq. (1)] appears to work well for representing the heat and moisture transport in stratocumulus clouds as well.

However, as indicated by Figs. 7i and 7j, no improvement is seen in the representation of total vertical momentum transport by the convective momentum fluxes due to the increased threshold of vertical velocity. This confirms that the poor representation of the total momentum fluxes in the cloud layer by the mass-flux approach is due to the fundamental difference in the physical processes that govern the vertical transport of conservative thermodynamic variables and nonconservative momentum components stated previously.

Although the mass-flux decomposition of fluxes using Eq. (1) can clearly reveal the difference between momentum and heat/moisture transport in the cloud layer (Figs. 3–7), the mass-flux top-hat profile used for decomposition oversimplifies the vertical transport induced by overturning circulations with different scales from small turbulent eddies to coherent convective cells. To better understand the transport processes in terms of scales, the LES-resolved vertical fluxes are also decomposed using 2D-FFT. A detailed description of 2D-FFT is provided in the appendix. The computed spectral energy from model output provides a way to examine the fidelity of the LESs performed in this study. Figure 9a shows an example of the normalized azimuthally integrated spectral energy of $u$, $v$, $w$, $\theta_l$, and $q_t$ at 290-m altitude averaged over the last 3 h from the simulation of the BOMEX case, where the definition of normalized azimuthally integrated spectral energy can be found in the appendix. In the inertial subrange, all spectra closely follow the Kolmogorov $-5/3$ power law (Kolmogorov 1941), suggesting that the LESs performed in this study capture the basic characteristics of atmospheric turbulence. It also shows that the magnitude of $w$ spectra in the energy-containing eddy range is substantially smaller than that of horizontal ($u$ and $v$) wind spectra. This result is consistent with previous studies (e.g., Kaimal et al. 1972, 1976; Busch 1973). Similar results are obtained in the simulations of other cases. Since the objective of this study is to investigate the vertical transport processes in moist convection, the presentation below will focus only on the cospectral analyses.

To better understand the differences between momentum transport and heat/moisture transport processes in the cloud layer, the phase relationship between vertical velocity and various variables is first examined. Figures 9b–e shows the azimuthal-mean phase spectra of $\overline{w'\theta_l'}$, $\overline{w'q_t'}$, $\overline{w'u'}$, and $\overline{w'v'}$ of the six cloud cases, where for the shallow cloud cases the phase spectra are averaged over the cloud layer defined by $\overline{q}_c > 0.001\,\mathrm{g\,kg^{-1}}$ in the last three simulation hours and the phase spectra of GATE and TOGA COARE are averaged over the cloud layers at 500–11 650 and 500–15 550 m in the convective episodes defined in Fig. 2, respectively. Also, to better compare the results, the phase spectra of $\overline{w'q_t'}$ shown in the figure are actually $180° - \Phi_{wq_t}(K)$. As shown in Figs. 3 and 4, the LES-resolved $\overline{w'\theta_l'}$ and $\overline{w'q_t'}$ are negative and positive in the cloud layer, respectively, and this is consistent with the phase spectral analyses that $\Phi_{w\theta_l}(K)$ and $\Phi_{wq_t}(K)$ are completely 180° out of phase in the BOMEX, RICO, ASTEX, and TOGA COARE cases. In the DYCOMS-II-RF01 and GATE cases, $\Phi_{w\theta_l}(K)$ and $\Phi_{wq_t}(K)$ are not completely out of phase, but the difference between $\Phi_{w\theta_l}(K)$ and $180° - \Phi_{wq_t}(K)$ is only about 10° and 5°, respectively. Ideally, two variables 180° out of phase, 90° out of phase, and 0° in phase will yield maximum negative, zero, and maximum positive covariance, respectively. The fact that $\Phi_{w\theta_l}(K)$ and $\Phi_{wq_t}(K)$ are greater and smaller than 90°, respectively, at all wavenumber indices suggests that all eddies tend to generate negative fluxes of $\overline{w'\theta_l'}$ and positive fluxes of $\overline{w'q_t'}$ to certain degrees depending on specific wavenumber indices. The phase spectra also show that $\Phi_{w\theta_l}(K)$ and $180° - \Phi_{wq_t}(K)$ have peaks approximately at wavenumber indices 50–60 for the BOMEX, RICO, ASTEX, GATE, and TOGA COARE cases, and wavenumber 10 for the DYCOMS-II-RF01 case. Since the phase peak values of $\Phi_{w\theta_l}(K)$ and $180° - \Phi_{wq_t}(K)$ are closer to 180°, it suggests that eddies in the vicinity of peak wavenumber indices are more efficient in generating negative and positive fluxes of $\overline{w'\theta_l'}$ and $\overline{w'q_t'}$ in the cloud layer. The phase spectra of momentum fluxes $\Phi_{wu}(K)$ and $\Phi_{wv}(K)$ are much more complicated and substantially different from $\Phi_{w\theta_l}(K)$ and $\Phi_{wq_t}(K)$. This

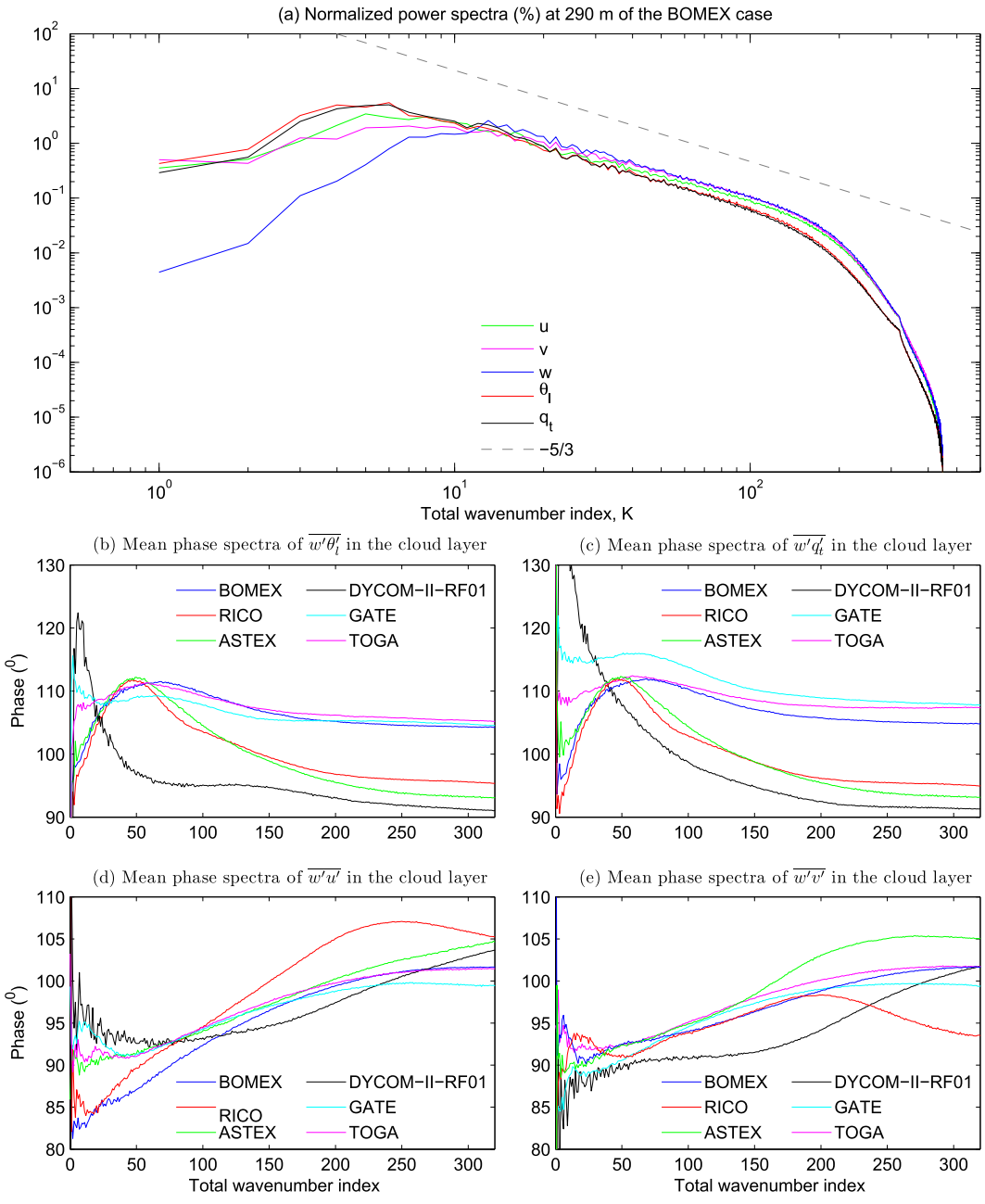


FIG. 9. (a) Normalized power spectra (%) of different variables at 290-m altitude of BOMEX averaged over the last three simulation hours. (b)–(e) Phase spectra averaged over the cloud layer and over the last three simulation hours for shallow cloud cases and the convective episode for deep cloud cases indicated in Fig. 2. Here, the cloud layer is defined by $q_c > 10^{-3}\,\mathrm{g\,kg^{-1}}$ for the shallow cloud cases. For deep cloud cases, the cloud layer is taken as 500–11 650 m for GATE and 500–15 550 m for TOGA COARE. Note that the phase spectrum of $\overline{w'q_t'}$ shown in the figure is actually $180° - \Phi_{wq_t}(kl)$.

may explain why vertical momentum transport behaves so differently from the vertical transport of conservative thermodynamic variables in the cloud layer.

Figure 10 shows the normalized azimuthally integrated cospectra $\tilde{C}_{w\theta_l|n}(K)$, $\tilde{C}_{wq_t|n}(K)$, $\tilde{C}_{wu|n}(K)$, and $\tilde{C}_{wv|n}(K)$ as function of the total wavenumber index $K$ averaged over the same layer and same period as that in Figs. 9b–e, where the definitions of $\tilde{C}_{w\theta_l|n}(K)$, $\tilde{C}_{wq_t|n}(K)$, $\tilde{C}_{wu|n}(K)$, and $\tilde{C}_{wv|n}(K)$ can be found in the appendix. To better illustrate the result, the scale of normalized cospectra has been nonlinearly adjusted and the accumulated normalized cospectra over three total

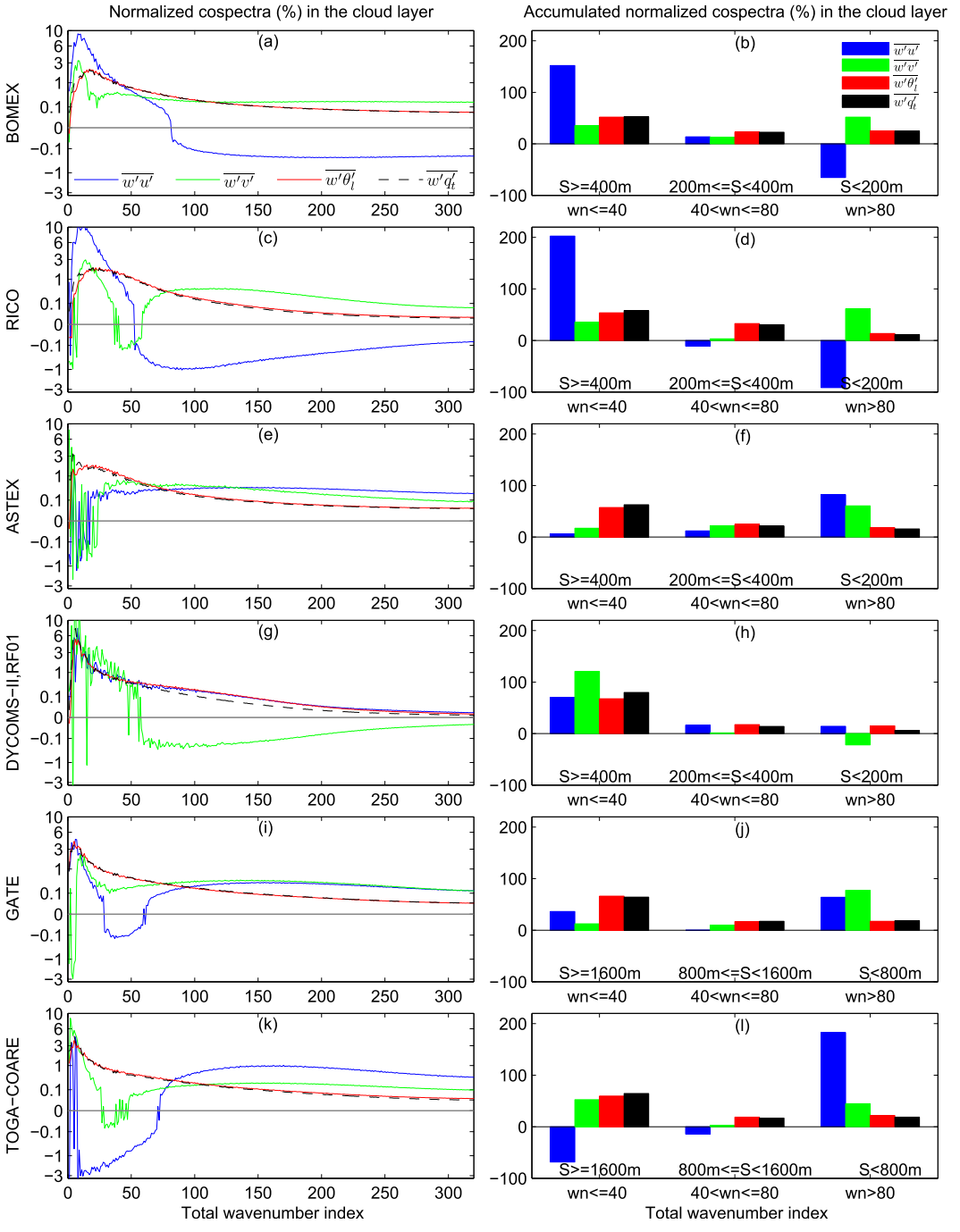


FIG. 10. (a),(c),(e),(g),(i),(k) Normalized cospectra (%) averaged over the same cloud layer and the time period as that defined by Fig. 9. (b),(d),(f),(h),(j),(l) Accumulated normalized cospectra (%) over three total wavenumber index ranges: 1–40, 41–80, and ≥81.

wavenumber index ranges (i.e., 1–40, 41–80, >81) are also provided. The 2D-FFT decomposition clearly shows that the normalized cospectra of $\overline{w'\theta_l'}$ and $\overline{w'q_t'}$ closely match each other with the peak at $K$ approximately 16 for the shallow cumulus cases (BOMEX, RICO, and ASTEX), 5 for the stratocumulus case (DYCOMS-II-RF01), and 6 for the deep convection cases (GATE and TOGA COARE). Since the length of model domain is 25 × 640 = 16 000 m for the shallow cloud cases and 100 × 640 = 64 000 m for the deep convection cases, these peak wavenumber indices correspond to the spatial scales of 1000 m for shallow

cumulus, 3200 m for stratocumulus, and 10 667 m for deep convection. The accumulated normalized cospectra clearly indicate that eddies with total wavenumber indices greater than 80 (or scales smaller than 200 m for shallow cloud cases and 800 m for deep cloud cases) contribute less than 25% to the total $\overline{w'\theta_l'}$ and $\overline{w'q_t'}$ for all cases. This result is consistent with the classic dynamic view of convection that coherent convective features are mainly responsible for the vertical transport of heat and moisture in cloud layer. However, as shown previously, the mass-flux decomposition may fail to capture the fundamental heat and moisture transport processes in the cloud layer of convection when the fraction of coherent convective elements is large. The likely cause for the failure is that the top-hat distribution oversimplifies the rich scale of eddy circulations associated with the convection.

The cospectra of momentum fluxes are not only substantially different from those of $\overline{w'\theta_l'}$ and $\overline{w'q_t'}$ but also show different characteristics for the $x$-direction and $y$-direction components of momentum fluxes depending on specific cloud cases. In the BOMEX case, motions with total wavenumber indices smaller than 40 (scales greater than 400 m) contribute more to $\overline{w'u'}$ than to $\overline{w'\theta_l'}$, $\overline{w'q_t'}$, and $\overline{w'v'}$, suggesting large-scale circulations including coherent convective features are very efficient in transporting $x$-direction momentum. However, the cospectra clearly indicate that smaller-scale eddies with total wavenumber indices greater than 80 (scales smaller than 200 m) transport the $x$-direction momentum in an opposite direction to that transported by large-scale eddies. The accumulated $x$-direction momentum flux generated by eddies smaller than 200 m has a negative contribution up to 60% to the total flux in the cloud layer (Fig. 10b). From the fundamental physics of downgradient diffusion perspective, the transport with opposite directions by small and large eddies suggests that the vertical distribution of $x$-direction wind $u$ in the cloud layer has complicated structures, and this is verified by the detailed examination of horizontal wind distribution in the cloud layer from the model output (not shown here). Since eddies smaller than 200 m also contribute nearly half of the total $y$-direction momentum fluxes, it suggests that small eddies are more efficient in carrying momentum than heat and moisture in the cloud layer of shallow cumulus. As discussed previously, this is because small-scale eddies are likely driven by local wind shear, which can lead to large $w'u'$ and $w'v'$ but not necessarily large $w'\theta_l'$ and $w'q_t'$ if small shear-driven eddies are generated within a large thermally driven plume or cell that possesses similar thermodynamic properties. Some of the momentum transport associated with high wavenumber eddies could be caused by gravity waves. How to appropriately parameterize the gravity wave–induced vertical momentum transport in large-scale models is an important issue, but it is beyond the scope this study. We shall tackle the related problems in our future study.

The RICO case shares the basic characteristics of the BOMEX case except that eddies with a total wavenumber index around 50 (scale of 320 m) have a negative contribution to the LES-resolved $\overline{w'v'}$ (Fig. 10c). Since perturbations of a variable are defined with respect to the domain-mean value, this result suggests that the perturbations of $y$-direction wind in different parts of the LES domain have different distribution patterns. This is understandable since momentum components are not conservative variables subjected to the pressure gradient force. In the ASTEX case, the negative contribution to $\overline{w'u'}$ no longer exists. Like the other two shallow cumulus cases, eddies smaller than 200 m are much more efficient in transporting both $x$-direction and $y$-direction momentum than thermodynamic quantities, but in the ASTEX case, small eddies also contribute positively to the $x$-direction momentum flux. Interestingly, both $x$-direction and $y$-direction momentum cospectra show large perturbations in the low total wavenumber indices smaller than 25. As discussed previously, this may be caused by the complicated variation of horizontal winds with respect to the domain-mean winds. The momentum cospectra of the stratocumulus case (DYCOMS-II-RF01) show different characteristics from those of shallow cumulus cases. Large-scale eddy circulations (with the total wavenumber indices smaller than 60) contribute a dominant proportion to the total momentum fluxes in both directions. The relative importance of small-scale eddies to the momentum fluxes is reduced. Small eddies contribute negatively to the total $\overline{w'v'}$, which is different from what we see in the shallow cumulus cases. This is probably due to the weak wind shear in this stratocumulus case.

The cospectra of deep convection cases do show a certain similarity to those of shallow cumulus cases in that eddies with high wavenumber indices contribute significantly to the momentum fluxes in both directions, although an absolute comparison in terms of scales is impossible since the model resolution used for simulating shallow and deep cloud cases are different. The main differences are in the low wavenumber indices. In the TOGA COARE cases, low wavenumber circulations have a large negative contribution to $\overline{w'u'}$, particularly in the total wavenumber indices from 75 to 10, which largely cancels the positive contribution to $\overline{w'u'}$ from smaller eddies. On the other hand, eddies with low wavenumber indices contribute positively to the total $\overline{w'u'}$ in the GATE case. In short, the cospectrum analyses shown in Fig. 10 indicate that small-scale eddies are the efficient momentum carrier because the perturbed vertical

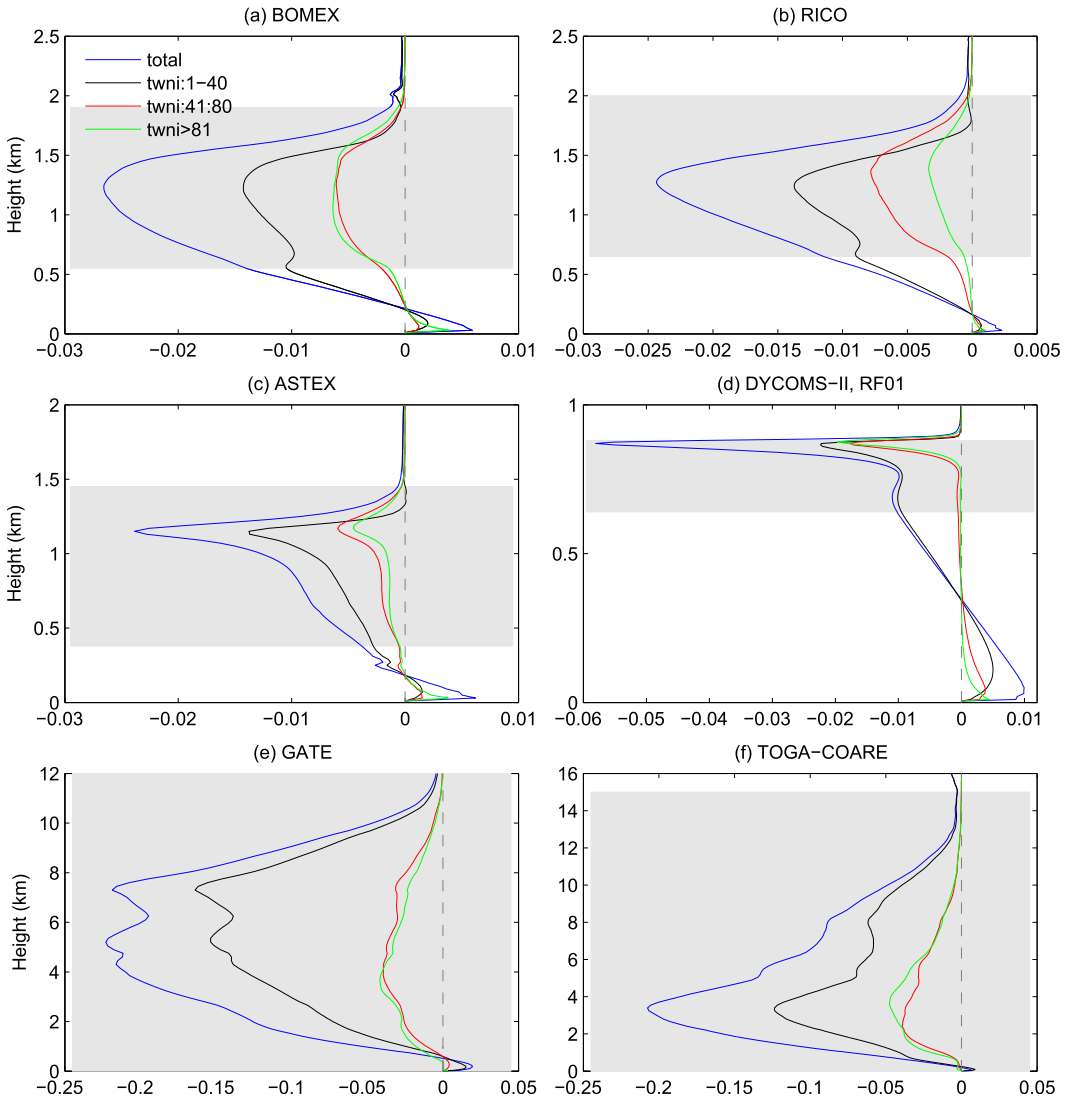


FIG. 11. Decomposition of the vertical fluxes of liquid water potential temperature (K m s$^{-1}$) by 2D-FFT of the six cloud cases. Blue, black, red, and green curves denote the total fluxes resolved by LES flux components accumulated over total wavenumber index 1–40, 41–80, and ≥81, respectively. The dashed line indicates the zero line. The profiles are averaged over the same period as that in Fig. 3. The shaded area indicates the cloud layer.

velocity and horizontal wind components associated with small-scale eddies are highly correlated. In addition, the vertical momentum transport is strongly case dependent since unlike conservative thermodynamic variables, which possess a certain vertical structure in a climate regime, the vertical and horizontal structures of wind components can vary substantially from case to case. This explains why the convective fluxes estimated by Eq. (3) cannot well represent the momentum transport in the cloud layer in the same way as it represents the vertical fluxes of conservative thermodynamic variables.

Figures 11 and 12 show the vertical profiles of the LES-resolved $\overline{w'\theta_l'}$ and $\overline{w'q_t'}$ and the 2D-FFT decomposed flux components accumulated over three total wavenumber index ranges: $K \le 40$, $40 < K \le 80$, and $K > 80$, where the shaded cloud layer is defined by $\overline{q}_c > 0.001\,\mathrm{g\,kg^{-1}}$. In the four shallow cloud cases, eddy circulations with $K$ smaller than 40 (or scales greater than 400 m) account for 80%–90% of the total fluxes of conversed thermodynamic variables in the upper-subcloud layer. In the cloud layer, the contribution from eddy circulations greater than 400 m drops to about 50% of the LES-resolved $\overline{w'\theta_l'}$ and $\overline{w'q_t'}$. This is understandable since lateral entrainment dilutes the convective plumes that originated at the surface as they rise. However, eddy circulations with scales greater than 200 m (or $K$ smaller than 80) account for more than 70%–80% of the LES-resolved $\overline{w'\theta_l'}$ and $\overline{w'q_t'}$ in the cloud

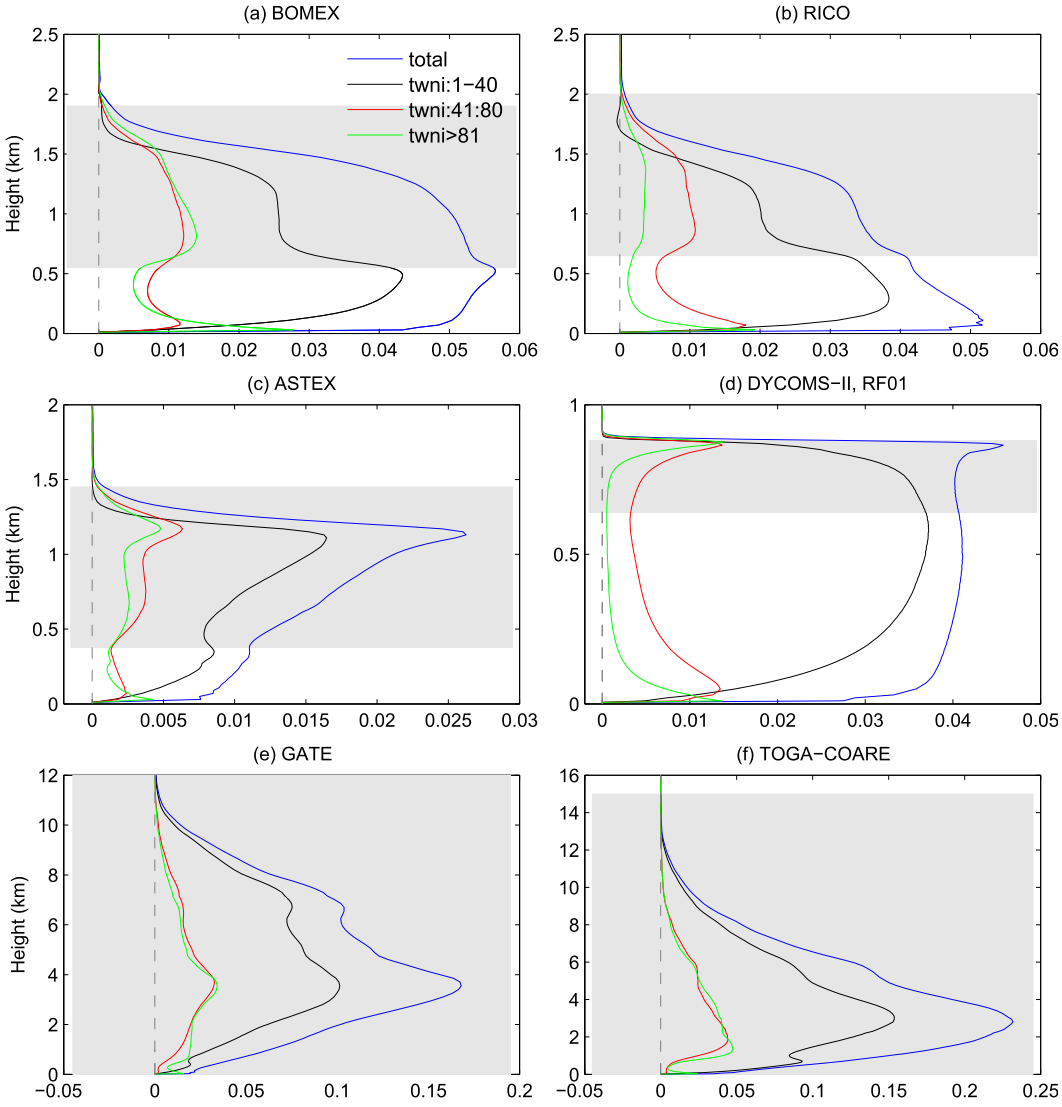


FIG. 12. As in Fig. 11, but for the vertical fluxes of the total water mixing ratio ($g\,kg^{-1}\,m\,s^{-1}$).

layer of shallow clouds. This is also true for the deep convection cases. In both shallow and deep cloud cases, the contribution of small eddies with $K$ greater than 80 to the LES-resolved $\overline{w'\theta_l'}$ and $\overline{w'q_t'}$ is insignificant throughout the vertical layer except for the surface layer. The 2D-FFT decomposition presented here basically supports the classic dynamic view of convection that coherent convective features are mainly responsible for the vertical transport of heat and moisture associated with convection.

The vertical profiles of momentum fluxes decomposed by 2D-FFT (Figs. 13 and 14) show much more complicated characteristics than those of $\overline{w'\theta_l'}$ and $\overline{w'q_t'}$. In the four shallow cloud cases, eddy circulations with $K$ smaller than 40 (scales greater than 400 m) appear to provide a good estimate of the LES-resolved momentum fluxes in both directions from the middle of the subcloud layer to the lower part of the cloud layer (except for the ASTEX case) but completely fail to represent the momentum fluxes in the upper part of the cloud layer. On the other hand, eddies with $K$ greater than 80 (scales smaller than 200 m) account for more than 50% of both $x$-direction and $y$-direction momentum fluxes in the upper part of the cloud layer, although their induced fluxes deviate substantially from the LES-resolved momentum fluxes in the lower part of the cloud layer. Note that in the BOMEX and RICO cases, the smaller-scale eddies with $K$ greater than 80 (scales smaller than 200 m) transport the $x$-direction momentum in an opposite direction to that transported by large eddies. The reason for this cancellation of momentum fluxes has been discussed previously. The 2D-FFT

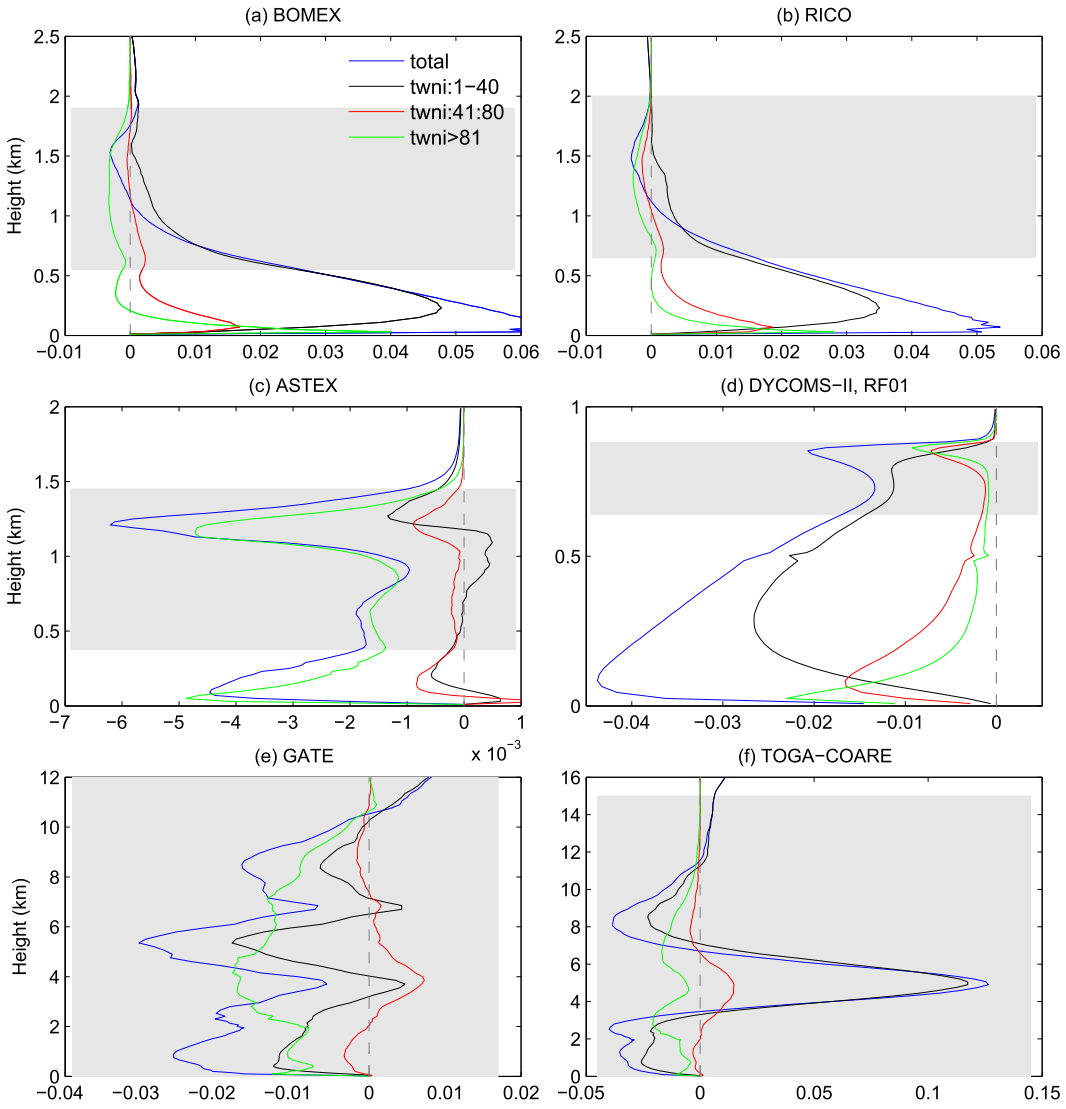


FIG. 13. As in Fig. 11, but for the vertical fluxes of the $x$-direction wind component ($m^2\,s^{-2}$).

decomposition of vertical momentum fluxes in the two deep convection cases show quite different characteristics. While the fluxes induced by the large-scale circulations appear to represent the LES-resolved momentum fluxes well in the cloud layer of the TOGA COARE case, they provide a poor estimate of momentum fluxes in the GATE case. This is likely because large convective cells do not necessarily conserve their momentum components, and thus the momentum transport by large eddies is case dependent. Small-scale eddy circulations also behave differently in transporting momentum in the two cases, but in both cases, they have a nonnegligible contribution to the total momentum transport in the cloud layer. Last, it should be pointed out that the vertical momentum flux profiles have a much more complicated structure than that of $\overline{w'\theta_l'}$ and $\overline{w'q_t'}$ and are different from case to case. As discussed previously, this may be explained by the fact that the vertical dynamic structure can change substantially even in the same climate regime in which the thermodynamic field shares similar characteristics.

## 4. Conclusions and discussion

How to appropriately represent the vertical transport processes associated with moist convection in large-scale models is a long standing problem in numerical weather forecasting and climate simulations. While the mass-flux approach provides a physical base for cumulus parameterization, under what conditions the convective fluxes formulated based on the mass-flux top-hat profile can represent the vertical transport of heat and moisture

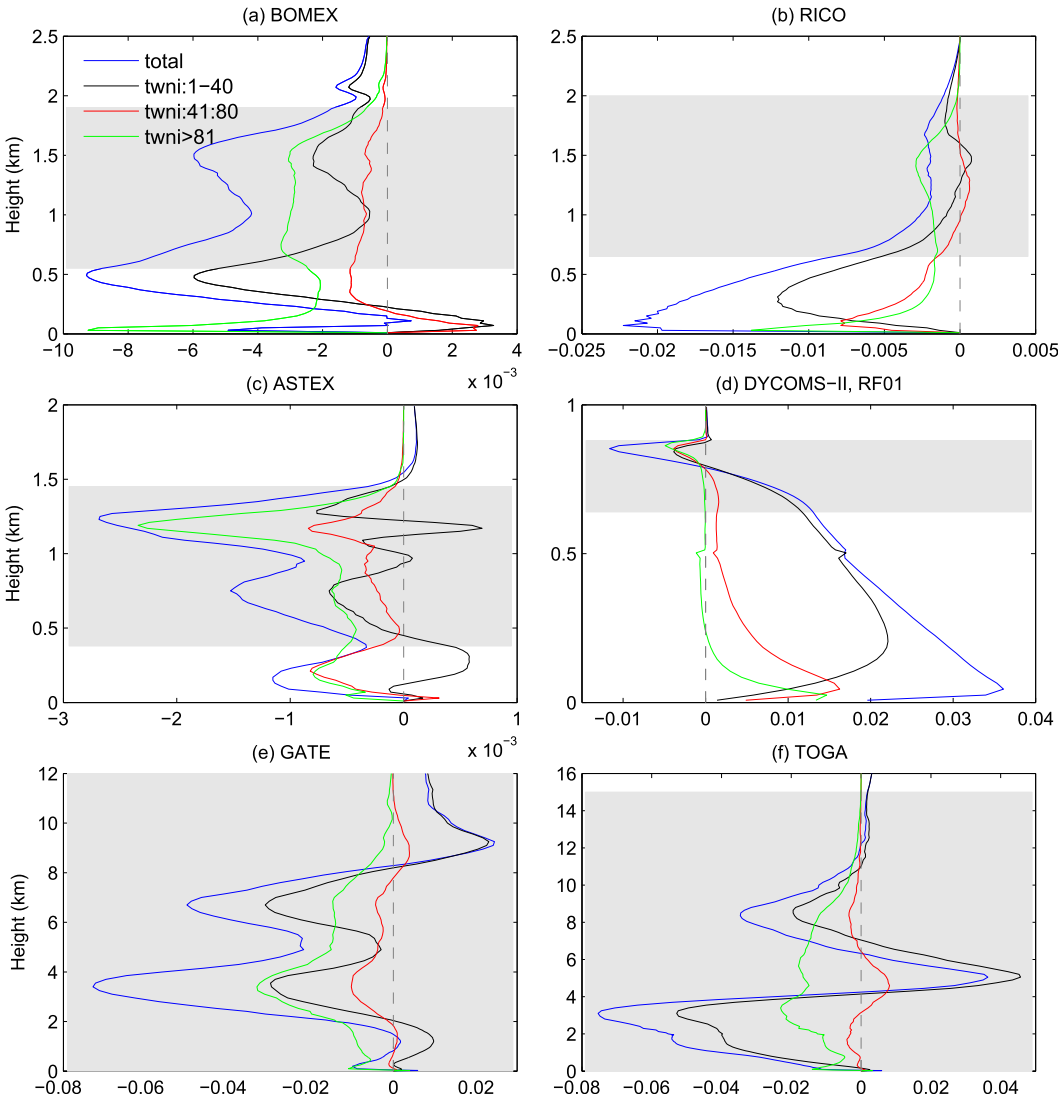


FIG. 14. As in Fig. 11, but for the vertical fluxes of the $y$-direction wind component ($m^2 s^{-2}$).

in the cloud layer and whether the same approach can be extended to the parameterization of momentum transport have not yet been thoroughly addressed. These two questions are investigated in this study using LESs of six well-documented cloud cases, including deep and shallow convective clouds as well as stratiform clouds. Two methods are used to decompose the LES-resolved vertical fluxes: the decomposition within the mass-flux framework in terms of coherent convective features defined by a top-hat profile and the decomposition by 2D-FFT in terms of wavenumbers. The main conclusions of this study are summarized as follows.

The convective fluxes computed based on the coherent cloud updraft can account for most of the vertical fluxes of conservative thermodynamic variables in the cloud layer for both shallow convective and stratiform cloud cases, consistent with previous studies. However, the simulations of the two deep convection cases, GATE and TOGA COARE, show that a good representation of the total vertical transport of conservative thermodynamic variables in the cumulus layer using the mass-flux approach requires an appropriate definition of the convective updraft since the convective fluxes computed based on the mass-flux formula depend strongly on the threshold of vertical velocity used for defining the convective updraft. While a too small threshold can smooth out the strong convective updrafts responsible for vertical transport by including too many weak updrafts, a too large threshold can eliminate some of the convective updrafts important for vertical transport. From the mass-flux decomposition perspective [i.e., Eq. (1)], the

former causes a large internal variation within the updrafts, whereas the latter leads to a large internal variation within the environmental downdrafts. In both cases, the inappropriately defined convective updraft can cause a significant underestimation of the total vertical transport in the cumulus layer by the mass-flux formula through unrealistically increasing the contribution of internal variation within the convective updrafts to the total transport in the former and increasing the environmental contribution in the latter, but both contributions from the internal variations within the convective updraft and environment are neglected in the mass-flux parameterization. This problem may be solved by the unified mass-flux framework recently proposed by Arakawa and Wu (2013) and Wu and Arakawa (2014) in which the convective updraft fraction can be predicted internally within the framework. If their method could appropriately account for the change in convective updraft fraction under different forcing conditions, then the mass-flux parameterization would be significantly improved. In a recent study, Liu et al. (2015) showed that the representation of convective transport can be significantly improved using multiple updrafts. This could provide another possible way to improve the mass-flux representation of convection-induced vertical transport.

All cloud cases investigated in this study show that the mass-flux approach provides a poor representation of vertical momentum transport in the cloud layer. The decomposition by 2D-FFT and other analyses suggest four reasons that might be responsible for the different behaviors between the vertical transport of conservative thermodynamic variables and nonconservative momentum components. First, compared with the conservative thermodynamic variables that possess relatively simple and sometimes well-defined vertical structure, the complicated momentum distribution in the cloud layer cannot be well described by the simple top-hat profile. Second, small-scale eddies are more efficient in carrying momentum than in carrying conservative thermodynamic variables in the cloud layer. This is because shear-driven small-scale eddies can generate highly correlated perturbations of vertical velocity and horizontal winds, resulting in large $w'u'$ and $w'v'$ but not necessarily large $w'\theta_l'$ and $w'q_t'$ if shear-driven small-scale eddies are generated in an environment that possesses similar thermodynamic properties. On the other hand, large thermally driven plumes or cells can generate large $w'\theta_l'$ and $w'q_t'$ since plumes or cells often possess similar thermodynamic properties that have an excellent correlation with the convective updrafts. However, thermally driven plumes or cells do not necessarily possess similar horizontal momentum, leading to large positive and negative momentum perturbations within convective plumes or cells depending on specific conditions. The cancellation of positive and negative $w'u'$ and $w'v'$ within the plume updrafts can result in small net momentum fluxes. Third, the phase relationship between vertical velocity and conservative thermodynamic variables is substantially different from that between vertical velocity and horizontal momentum components. Finally, while the vertical thermodynamic structure shares similar characteristics in the same climate regime, the structure of horizontal momentum can change substantially from case to case even in the same climate regime. The combined effects of all these factors cause the vertical momentum transport in the cloud layer induced by eddies with various scales to be too complicated to be described by the simple dynamic view of mass-flux approach.

*Acknowledgments.* This work is supported by the National Science Foundation under Grant AGS-0847332 and the BP-sponsored Gulf of Mexico Research Initiative. The author is very grateful to the three anonymous reviewers for their constructive comments, as their helpful suggestions led to improvements in this paper. All data used in this study can be accessed online (http://vortex.ihrc.fiu.edu/download/momentum_transport/).

## APPENDIX

### 2D-FFT

Let $w(m, n)$ and $\chi(m, n)$ be the vertical velocity and a generic scalar on a 2D model grid at an arbitrary height, where $m = 0, 1, \ldots, M-1$ and $n = 0, 1, \ldots, N-1$ are the model grid number indices and $M$ and $N$ are the number of model grids in $x$ and $y$ directions, respectively (for this study, $M = N = 640$). The 2D-FFT of $w(m, n)$ and $\chi(m, n)$, then, may be written as

$$\hat{w}(k,l) = \frac{1}{NM}\sum_{m=0}^{M-1}\sum_{n=0}^{N-1} w(m,n)e^{-i(\omega_k m+\omega_l n)} \quad \text{and} \qquad \text{(A1)}$$

$$\hat{\chi}(k,l) = \frac{1}{NM}\sum_{m=0}^{M-1}\sum_{n=0}^{N-1} \chi(m,n)e^{-i(\omega_k m+\omega_l n)}, \qquad \text{(A2)}$$

where $k$ and $l$ are the 2D-FFT wavenumber indices in the $x$ and $y$ directions, respectively; and $\omega_k = 2\pi(k/M), k = [-(M/2)\colon 1\colon (M/2) - 1], \omega_l = 2\pi(l/N)$, and $l = [-(N/2)\colon 1\colon (N/2) - 1]$. The terms $\omega_k/\Delta x$ and $\omega_l/\Delta y$ are the angular wavenumbers in the $x$ and $y$ directions, respectively. In this study, $\Delta x = \Delta y = 25$ m for shallow cloud cases and $\Delta x = \Delta y = 100$ m for deep

convective cloud cases. The spectral energy, then, may be written as

$$E_w(k,l) = \hat{w}(k,l)^* \cdot \hat{w}(k,j) = |\hat{w}(k,l)|^2 \quad \text{and}$$
$$E_\chi(k,l) = \hat{\chi}(k,l)^* \cdot \hat{\chi}(k,j) = |\hat{\chi}(k,l)|^2, \tag{A3}$$

where the asterisk denotes the complex conjugate. One may also define the cross spectrum between $w(m, n)$ and $\chi(m, n)$ as

$$\begin{aligned} G_{w\chi}(k,l) &= \hat{w}(k,l)^* \cdot \hat{\chi}(k,j) \\ &= [\hat{w}(k,l)_r - i\hat{w}(k,l)_i][\hat{\chi}(k,l)_r + i\hat{\chi}(k,l)_i] \\ &= [\hat{w}(k,l)_r \cdot \hat{\chi}(k,l)_r + \hat{w}(k,l)_i \cdot \hat{\chi}(k,l)_i] \\ &\quad - i[\hat{w}(k,l)_i \cdot \hat{\chi}(k,l)_r - \hat{w}(k,l)_r \cdot \hat{\chi}(k,l)_i] \\ &= C_{w\chi}(k,l) - iQ_{w\chi}(k,l), \end{aligned} \tag{A4}$$

where the subscripts $r$ and $i$ indicate the real and imaginary parts of a complex, respectively. the terms $C_{w\chi}(k, l)$ and $Q_{w\chi}(k, l)$ are known as the cospectrum and quadrature spectrum, respectively. Parseval's theorem states that the sum of spectral energy and cospectral amplitudes over all 2D-FFT harmonics equals the variance of $w(m, n)$ and $\chi(m, n)$ and the covariance between them, respectively; that is,

$$\sum_{k=0}^{M-1}\sum_{l=0}^{N-1} E_w(k,l) = \overline{w'^2}, \quad \sum_{k=0}^{M-1}\sum_{l=0}^{N-1} E_\chi(k,l) = \overline{\chi'^2}, \quad \text{and}$$
$$\sum_{k=0}^{M-1}\sum_{l=0}^{N-1} C_{w\chi}(k,l) = \overline{w'\chi'}. \tag{A5}$$

While $C_{w\chi}(k, l)$ provides a way to decompose a vertical flux in terms of 2D-FFT harmonics, the quadrature spectrum, $Q_{w\chi}(k, l)$, describes the phase relationship between the two variables. The phase spectrum, then, may be defined as

$$\Phi_{w\chi}(k,l) = 180^0 - \tan^{-1}\left[\frac{Q_{w\chi}(k,l)}{C_{w\chi}(k,l)}\right], \tag{A6}$$

where $\Phi_{w\chi}(k, l)$ can be interpreted as the phase difference between $w(m, n)$ and $\chi(m, n)$ that yields the greatest correlation for any wavenumber index, $k$ and $l$. The terms $E_w(k, l)$, $E_\chi(k, l)$, $C_{w\chi}(k, l)$, and $\Phi_{w\chi}(k, l)$ are the spectra on a 2D plane $\{k = [-(M/2)\colon 1\colon (M/2) - 1]$ and $l = [-(N/2)\colon 1\colon (N/2) - 1]\}$ centered at wavenumber 0. To better display the result of spectral analyses, define a total wavenumber index $K = \sqrt{k^2 + l^2}$ then the obtained spectra in a Cartesian coordinate $(k, l)$ may be rewritten in a polar coordinate $(K, \varphi)$. This allows one to define azimuthally integrated spectral energy and cospectrum, that is, $\tilde{E}_w(K) = \sum_{\phi=0}^{2\pi} E_w(K, \phi)$, $\tilde{E}_\chi(K) = \sum_{\phi=0}^{2\pi} E_\chi(K, \phi)$, and $\tilde{C}_{w\chi}(K) = \sum_{\phi=0}^{2\pi} C_{w\chi}(K, \phi)$, satisfying $\sum_K \tilde{E}_w(K) = \overline{w'^2}$, $\sum_K \tilde{E}_\chi(K) = \overline{\chi'^2}$, and $\sum_K \tilde{C}_{w\chi}(K) = \overline{w'\chi'}$, and an azimuthally averaged phase spectrum $\overline{\Phi}_{w\chi}(K)$. One may further define normalized spectral energy and cospectrum as $\tilde{E}_{w|n}(K) = [\tilde{E}_w(K)/\overline{w'^2}]$, $\tilde{E}_{\chi|n}(K) = [\tilde{E}_\chi(K)/\overline{\chi'^2}]$, and $\tilde{C}_{w\chi|n}(K) = [\tilde{C}_{w\chi}(K)/\overline{w'\chi'}]$, which provide a quantitative measure of the individual contributions of motions with different wavenumbers to the total variance $\overline{w'^2}$, $\overline{\chi'^2}$, and flux $\overline{w'\chi'}$ in percentage. In this study, to calculate the azimuthally integrated spectral energy and cospectrum and azimuthally averaged phase spectrum, the 2D-FFT-determined spectral energy, cospectra, and phase spectra, $E_w(k, l)$, $E_\chi(k, l)$, $C_{w\chi}(k, l)$, and $\Phi_{w\chi}(k, l)$, respectively, on a 2D plane are binned into the discretized total wavenumber indices $K$ from 1 to 452 with an increment of 1 . All wavenumber indices greater than 452 are grouped into 452.

## REFERENCES


Arakawa, A., and W. H. Schubert, 1974: Interaction of a cumulus cloud ensemble with the large-scale environment, part I. *J. Atmos. Sci.*, **31**, 674–701, doi:10.1175/1520-0469(1974)031<0674:IOACCE>2.0.CO;2.

——, and C.-M. Wu, 2013: A unified representation of deep moist convection in numerical modeling of the atmosphere. Part I. *J. Atmos. Sci.*, **70**, 1977–1992, doi:10.1175/JAS-D-12-0330.1.

Bradshaw, P., 1967: Inactive motion and pressure fluctuations in turbulent boundary layers. *J. Fluid Mech.*, **30**, 241–258, doi:10.1017/S0022112067001417.

Bretherton, C. S., S. K. Krueger, M. C. Wyant, P. Bechtold, E. van Meijgaard, B. Stevens, and J. Teixeira, 1999: A GCSS boundary layer model intercomparison study of the first ASTEX Lagrangian experiment. *Bound.-Layer Meteor.*, **93**, 341–380, doi:10.1023/A:1002005429969.

Bryan, G. H., J. C. Wyngaard, and J. M. Fritsch, 2003: Resolution requirements for the simulation of deep moist convection. *Mon. Wea. Rev.*, 131, 2394–2416, doi:10.1175/1520-0493(2003)131<2394:RRFTSO>2.0.CO;2.

Busch, N. E., 1973: The surface boundary layer (Part I). *Bound.-Layer Meteor.*, **4**, 213–240, doi:10.1007/BF02265234.

Grabowski, W. W., X. Wu, and M. W. Moncrieff, 1996: Cloud-resolving modeling of tropical cloud system during phase III of GATE. Part I: Two-dimensional experiments. *J. Atmos. Sci.*, **53**, 3684–3709, doi:10.1175/1520-0469(1996)053<3684:CRMOTC>2.0.CO;2.

Högström, U., and H. Bergström, 1996: Organized turbulence structures in the near-neutral atmospheric surface layer. *J. Atmos. Sci.*, **53**, 2452–2464, doi:10.1175/1520-0469(1996)053<2452:OTSITN>2.0.CO;2.

Houze, R. A., Jr., 1973: A climatological study of vertical transports by cumulus-scale convection. *J. Atmos. Sci.*, **30**, 1112–1123, doi:10.1175/1520-0469(1973)030<1112:ACSOVT>2.0.CO;2.

Kaimal, J. C., J. C. Wyngaard, Y. Izumi, and O. R. Coté, 1972: Spectral characteristics of surface-layer turbulence. *Quart. J. Roy. Meteor. Soc.*, **98**, 563–589, doi:10.1002/qj.49709841707.

——, ——, D. A. Haugen, O. R. Coté, Y. Izumi, S. J. Caughey, and C. J. Readings, 1976: Turbulence structure in the convective boundary layer. *J. Atmos. Sci.*, **33**, 2152–2169, doi:10.1175/1520-0469(1976)033<2152:TSITCB>2.0.CO;2.

Kershaw, R., and D. Gregory, 1997: Parameterization of momentum transport by convection. I: Theory and cloud modelling results. *Quart. Roy. Meteor. Soc.*, **123**, 1133–1151, doi:10.1002/qj.49712354102.

Khairoutdinov, M. F., and D. A. Randall, 2003: Cloud resolving modeling of the ARM summer 1997 IOP: Model formulation, results, uncertainties, and sensitivities. *J. Atmos. Sci.*, **60**, 607–625, doi:10.1175/1520-0469(2003)060<0607:CRMOTA>2.0.CO;2.

——, S. K. Krueger, C.-H. Moeng, P. A. Bogenschutz, and D. A. Randall, 2009: Large-eddy simulation of maritime deep tropical convection. *J. Adv. Model. Earth Syst.*, **1**, 15, doi:10.3894/JAMES.2009.1.15.

Kolmogorov, A. N., 1941: Energy dissipation in local isotropic turbulence. *Dokl. Akad. Nauk SSSR*, **32**, 19–21.

LeMone, M. A., and E. J. Zipser, 1980: Cumulonimbus vertical velocity events in GATE. Part I: Diameter, intensity and mass flux. *J. Atmos. Sci.*, **37**, 2444–2457, doi:10.1175/1520-0469(1980)037<2444:CVVEIG>2.0.CO;2.

Liu, Y.-C., J. Fan, G. J. Zhang, K.-M. Xu, and S. J. Ghan, 2015: Improving representation of convective transport for scale-aware parameterization: 2. Analysis of cloud-resolving model simulations. *J. Geophys. Res. Atmos.*, **120**, 3510–3532, doi:10.1002/2014JD022145.

Mahrt, L., and W. Gibson, 1992: Flux decomposition into coherent structures. *Bound.-Layer Meteor.*, **60**, 143–168, doi:10.1007/BF00122065.

Mason, B. J., 1975: The GARP Atlantic tropical experiment. *Nature*, **255**, 17–20, doi:10.1038/255017a0.

Mechem, D. B., and A. J. Oberthaler, 2013: Numerical simulation of tropical cumulus congestus during TOGA COARE. *J. Adv. Model. Earth Syst.*, **5**, 623–637, doi:10.1002/jame.20043.

Redelsperger, J.-L., and Coauthors, 2000: A GCSS model intercomparison for a tropical squall line observed during TOGA-COARE. I: Cloud-resolving models. *Quart. J. Roy. Meteor. Soc.*, **126**, 823–864, doi:10.1002/qj.49712656404.

Riehl, H., and D. Soltwisch, 1974: On the depth of the friction layer and the vertical transfer of momentum in the trades. *Beitr. Phys. Atmos.*, **47**, 56–66.

Schneider, E. K., 1975: The Hadley circulation of the Earth's atmosphere. Ph.D. thesis, Harvard University, 285 pp.

——, and R. S. Lindzen, 1976: A discussion of the parameterization of momentum exchange by cumulus convection. *J. Geophys. Res.*, **81**, 3158–3160, doi:10.1029/JC081i018p03158.

Shaw, W. J., and J. A. Businger, 1985: Intermittency and the organization of turbulence in the near-neutral marine atmospheric boundary layer. *J. Atmos. Sci.*, **42**, 2563–2584, doi:10.1175/1520-0469(1985)042<2563:IATOOT>2.0.CO;2.

Siebesma, A. P., and J. W. M. Cuijpers, 1995: Evaluation of parametric assumptions for shallow cumulus convection. *J. Atmos. Sci.*, **52**, 650–666, doi:10.1175/1520-0469(1995)052<0650:EOPAFS>2.0.CO;2.

Song, X., X. Wu, G. J. Zhang, and R. Arritt, 2008: Dynamical effects of convective momentum transports on global climate simulations. *J. Climate*, **21**, 180–194, doi:10.1175/2007JCLI1848.1.

Stevens, and Coauthors, 2005: Evaluation of large-eddy simulations via observations of nocturnal marine stratocumulus. *Mon. Wea. Rev.*, **133**, 1443–1462, doi:10.1175/MWR2930.1.

Stone, P. H., W. J. Quirk, and R. C. J. Somerville, 1974: The effect of small-scale vertical mixing of horizontal momentum in a general circulation model. *Mon. Wea. Rev.*, **102**, 765–771, doi:10.1175/1520-0493(1974)102<0765:TEOSSV>2.0.CO;2.

Townsend, A. A., 1961: Equilibrium layers and wall turbulence. *J. Fluid Mech.*, **11**, 97–120, doi:10.1017/S0022112061000883.

Tung, W.-W., and M. Yanai, 2002a: Convective momentum transport observed during the TOGA COARE IOP. Part I: General features. *J. Atmos. Sci.*, **59**, 1857–1871, doi:10.1175/1520-0469(2002)059<1857:CMTODT>2.0.CO;2.

——, and ——, 2002b: Convective momentum transport observed during the TOGA COARE IOP. Part II: Case studies. *J. Atmos. Sci.*, **59**, 2535–2549, doi:10.1175/1520-0469(2002)059<2535:CMTODT>2.0.CO;2.

VanZanten, M. C., and Coauthors, 2011: Controls on precipitation and cloudiness in simulations of trade-wind cumulus as observed during RICO. *J. Adv. Model. Earth Syst.*, **3**, M06001, doi:10.1029/2011MS000056.

Wang, S., and B. Stevens, 2000: Top-hat representation of turbulence statistics in cloud-topped boundary layers: A large-eddy simulation study. *J. Atmos. Sci.*, **57**, 423–441, doi:10.1175/1520-0469(2000)057<0423:THROTS>2.0.CO;2.

Webster, P. J., and R. Lukas, 1992: TOGA COARE: The Coupled Ocean–Atmosphere Response Experiment. *Bull. Amer. Meteor. Soc.*, **73**, 1377–1416, doi:10.1175/1520-0477(1992)073<1377:TCTCOR>2.0.CO;2.

Wu, C.-M., and A. Arakawa, 2014: A unified representation of deep moist convection in numerical modeling of the atmosphere. Part II. *J. Atmos. Sci.*, **71**, 2089–2103, doi:10.1175/JAS-D-13-0382.1.

Wu, X., and M. Yanai, 1994: Effects of vertical wind shear on the cumulus transport of momentum: Observations and parameterization. *J. Atmos. Sci.*, **51**, 1640–1660, doi:10.1175/1520-0469(1994)051<1640:EOVWSO>2.0.CO;2.

——, W. W. Grabowski, and W. M. Moncrieff, 1998: Long-term behavior of cloud systems in TOGA COARE and their interactions with radiative and surface processes. Part I: Two-dimensional modeling study. *J. Atmos. Sci.*, **55**, 2693–2714, doi:10.1175/1520-0469(1998)055<2693:LTBOCS>2.0.CO;2.

——, L. Deng, X. Song, and G.-J. Zhang, 2007: Coupling of convective momentum transport with convective heating in global climate simulations. *J. Atmos. Sci.*, **64**, 1334–1349, doi:10.1175/JAS3894.1.

Xu, K.-M., and D. A. Randall, 1996: Explicit simulation of cumulus ensembles with the GATE phase III data: Comparison with observations. *J. Atmos. Sci.*, **53**, 3710–3736, doi:10.1175/1520-0469(1996)053<3710:ESOCEW>2.0.CO;2.

Zhang, G. J., and H.-R. Cho, 1991a: Parameterization of the vertical transport of momentum by cumulus clouds. Part I: Theory. *J. Atmos. Sci.*, **48**, 1483–1492, doi:10.1175/1520-0469(1991)048<1483:POTVTO>2.0.CO;2.

——, and ——, 1991b: Parameterization of the vertical transport of momentum by cumulus clouds. Part II: Application. *J. Atmos. Sci.*, **48**, 2448–2457, doi:10.1175/1520-0469(1991)048<2448:POTVTO>2.0.CO;2.

——, and X. Wu, 2003: Convective momentum transport and perturbation pressure field from a cloud-resolving model simulation. *J. Atmos. Sci.*, **60**, 1120–1139, doi:10.1175/1520-0469(2003)060<1120:CMTAPP>2.0.CO;2.

Zhu, P., and Coauthors, 2005: Intercomparison and interpretation of single-column model simulations of a nocturnal stratocumulus-topped marine boundary layer. *Mon. Wea. Rev.*, **133**, 2741–2758, doi:10.1175/MWR2997.1.

——, J. A. Zhang, and F. J. Masters, 2010: Wavelet analyses of turbulence in the hurricane surface layer during landfalls. *J. Atmos. Sci.*, **67**, 3793–3805, doi:10.1175/2010JAS3437.1.